DUCTILE MACHINING OF CRYSTALLINE MATERIALS WITH VARIABLE RAKE SINGLE POINT DIAMOND MACHINING

by

Adam Daniel Griffin

A thesis submitted to the faculty of
The University of North Carolina at Charlotte
in partial fulfillment of the requirements
for the degree of Master of Science in
Mechanical Engineering

Charlotte

2019

Approved by:

Dr. Christopher Evans

Dr. Matthew Davies

Dr. Joseph Owen

ABSTRACT

ADAM DANIEL GRIFFIN. Ductile machining of crystalline materials with variable rake single point diamond machining. (Under the direction of DR. CHRISTOPHER EVANS)

The effect of a variable rake machining process such as Fast Tool Servo (FTS) on optical IR crystalline materials isn't well understood and can be difficult to test. This thesis proposes and develops the concept of using a 'starburst' cut geometry to facilitate the optimization of diamond geometry and cutting parameter choice. This process is then applied in an industrial setting to manufacture hex packed lens arrays of 1mm sag and 30° max slope.

TABLE OF CONTENTS

LIST OF FIGURES

NOMENCLATURE

FTS – Fast Tool Servo

STS – Slow Tool Servo

Ductile Cutting – Shorthand for describing a form of machining crystalline materials that leaves no evidence of brittle fracture

Effective Rake Angle – The rake angle of the diamond tool as compared to the normal vector of the local surface

Rake Bias – An FTS mounted diamond transiting a feature will encounter a range of effective rake angles. Using a negative rake diamond will bias this effective rake angle range negative.

C axis mode – The Precitech Nanoform 250 Ultra used to perform the cuts described in this thesis is equipped with a spindle that can be operated in two modes: spindle and axis. In spindle mode, the spindle is commanded to maintain a given RPM speed. In axis mode, the spindle is commanded to go to a given position at a given angular speed. Repeated commands to go to a new position at a given speed can mimic the effects of constant rotation. Rotating this way in C axis mode reduces the maximum rotation speed but increases positional accuracy.

Field – The flat area surrounding lenses or other cut geometry. The field generally represents a single plane normal to the spindle axis.

CHAPTER 1: INTRODUCTION

Surface roughness is an important property that affects the function of most machined parts. It is one of the primary factors affecting the reflectance and scattering of optical surfaces. (Donovan, Ashley, & Bennett, 1963) The ability to single point diamond machine IR transmissive crystals such as silicon and germanium with low surface roughness is one of the technologies that enable production of aspheric and other types of freeform IR lenses.

A primary source of surface roughness in machined brittle materials is a fracturing of the surface during machining. The correlation of fracturing on a surface to its measured roughness depends on the method of measurement and analysis. The two primary methods of measuring surface roughness are contact profilometry and non-contact interferometry.

Typical methods of contact profilometry use a stylus probe with a tip of known radius. As the stylus moves along the surface, the profile measured is a convolution of the true surface and the radius of the stylus tip. This convolution effectively places a lower bound on the spatial periods capable of being measured (or upper bound on the spatial frequency). This spatial period limit is generally assumed to be equal to the radius of the stylus. Electronic and sources of other high frequency noise can be removed from the measured profile (if data point spacing is less than stylus radius) by filtering with a cutoff at the spatial period of the stylus radius and subtracting the remaining high-frequency profile from the original profile. Contact profilometry also has an effective limit to the slope it can measure due to the stylus tip being a cone with a

radius point. A surface fracture with a slope steeper than this cone will strike the flank of the stylus instead of the radius. As the stylus moves across this steep fracture, the flank of the stylus will cause the measured profile to have an incorrect slope. This will also have a smoothing effect, making the fracture appear more gradual than it really is.

The workhorse for non-contact interferometric measurement of roughness is scanning white light interferometry (SWLI). This method also has an implicit high frequency filtering effect due to the pixel spacing of measurement. The smallest measurable spatial period (or highest frequency) is twice the pixel spacing as determined by the Nyquist frequency. Higher frequencies can be measured by reducing pixel spacing by increasing objective magnification at the cost of reduced measurement area. SWLI also has a limit to the surface slope it can measure. SWLI relies on light reflected from the surface being measured. If a steep fracture on a surface causes the angle of the reflected light to exceed the numerical aperture of the objective, the light will not reenter the microscope. The area of this fracture will then have no data and be missing from the dataset.

The theoretical basis for the formation of this fracture has its roots in the mechanics of indentation fracture. A review paper by P. Ostojic et al. (Ostojic & McPherson, 1987) covers the history of models of fracture mechanics including crack initiation & propagation and subsurface damage. Lawn et al. were able to determine that sub-surface cracks formed prior to surface cracks. Their model required a uniform indenter contact pressure, but further investigations showed this assumption only held for sharp indenters with an angle of less than 90° and materials with a high ratio of

Young's modulus to yield stress. This work led to Lambropoulos et al. showing that Young's modulus, hardness, and fracture toughness must all be used to correlate glass mechanical properties with surface finish machined with deterministic grinding. (Lambropoulos, et al., 1996) This is in contrast to earlier work done with lapping that showed only hardness was needed to correlate material properties to surface finish. (Buijs & Korpel-van Houten, 1993)

Nakasuji et al. introduced the idea of using the ratio of resolved shear stress to the resolved tensile stress to correlate the locations of ductile cutting and brittle fracture on turned single crystals of germanium, silicon, and $LiNbO_3$. (Nakasuji, Hara, Matsunaga, lkawa, & Shirnada, 1990) The concept of a maximum depth of cut or critical chip thickness in cutting germanium and silicon was introduced by Blake & Scattergood. (Blake & Scattergood, 1990) This was later expanded upon to account for the depth of the surface damage. (Blackley & Scattergood, 1991) The model proposed by Blackley & Scattergood shows an increasing critical chip thickness with increasing diamond rake angle up to at least -30°. This model explains the ductile to brittle transition of machining configurations that maintain a fixed diamond rake angle.

There are other machining configurations such as slow tool servo (STS) and fast tool servo (FTS) that provide another method to cut optical freeforms. (Patterson & Magreb, 1985) (Davis, Roblee, & Hedges, 2009) In these configurations, the diamond is set up like a two-axis facing cut, but the Z axis is actuated during the spiral cut to create a freeform shape. This motion relative to the work causes a change in the effective rake of the diamond tool as it cuts the material.

The effect of a variable rake machining process on optical IR crystalline materials isn't well understood and can be difficult to test. Cutting lenses directly using typical negative rake diamonds results in radial slope gradients which would cause 'plowing' of the material where the material compression normally caused by a negative rake isn't achieved. Cutting high slopes over a large area requires longer cut times due to the volume of material needing to be removed.

This thesis demonstrates the use of a constant-maximum-slope three-dimensional sine wave annulus or 'starburst' pattern to test high effective rake angle variation while eliminating radial gradients and minimizing material removal. It also reviews evaluation techniques to determine if ductile cutting was achieved.

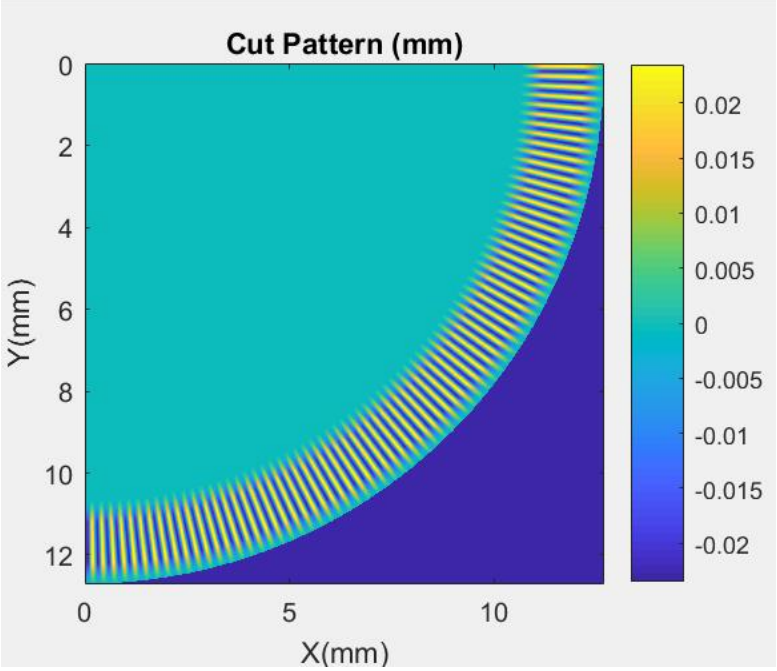

FIGURE 1: Simulated quadrant of 'starburst' test geometry

FIGURE 1 shows a simulation of one quadrant of the starburst geometry cut into a disc.

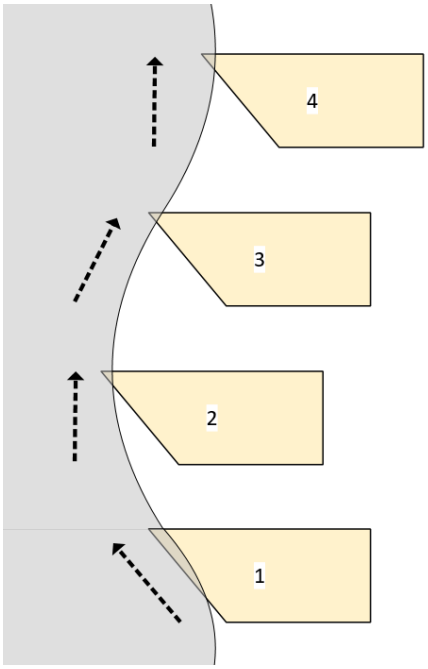

FIGURE 2: Example tool path in tangential direction

FIGURE 2 shows a tangential profile tool path of a nominal 0° rake diamond cutting the shape in FIGURE 1. In position 1 the effective rake angle is positive, conventionally described in a coordinate system where the surface normal vector is rotated positive (CCW) out of the plane of the rake face. In positions 2 and 4 the effective rake angle is 0° and in position 3 the effective rake angle is negative.

The effective rake at position 3 should be the location with the largest negative rake bias, largest critical chip thickness, and 'easiest' location to achieve ductile cutting. Therefore, the effective rake at position 1 should be the location with the largest positive rake bias, smallest critical chip thickness, and most 'difficult' location to achieve ductile cutting.

Confirmation of successful ductile cutting will focus on evaluating the surface texture of the starburst shape near position 1 at each oscillation.

CHAPTER 2: EXPERIMENTAL DESIGN

To maintain a constant maximum slope at every radius within the starburst annulus, the amplitude of the sine wave must be scaled slightly to account for the varying circumference. Within this annulus, the geometry is defined according to Equation (1):

$$Z = \frac{A_{max} * R}{R_{max}} * \sin(N * \theta) \quad (1)$$

Where Z is the resulting height, R and θ are the radial and tangential polar coordinates of the part, respectively. R_{max} is the outer radius of the annulus, N is the number of oscillations per revolution of the annulus, and A_{max} is the maximum amplitude of the sine wave occurring at the outer edge. A_{max} is given by Equation (2):

$$A_{max} = \tan(\varphi_{const}) * \frac{R_{max}}{N} \quad (2)$$

Combining Equation (1) and Equation (2) gives the closed form polar formula for the cut geometry within the annulus as Equation (3):

$$Z = \frac{R}{N} * \tan(\varphi_{const}) * \sin(N * \theta) \quad (3)$$

A blend geometry region was allocated outside the outer radius of the annulus and inside the inner radius of the annulus in which Equation (3) was used along with a weighting term that was 1 when adjacent to the annulus, and 0 when at the prescribed blended width from the annulus.

All the samples machined for this work were produced using a Precitech FastCom FTS 1000 mounted on a Precitech Nanoform 250 Ultra diamond turning machine. Example machine shown in FIGURE 3.

FIGURE 3: Precitech Nanoform 250 Ultra & FastCom FTS Controller

The specific arrangement used for this paper is shown below in FIGURE 4.

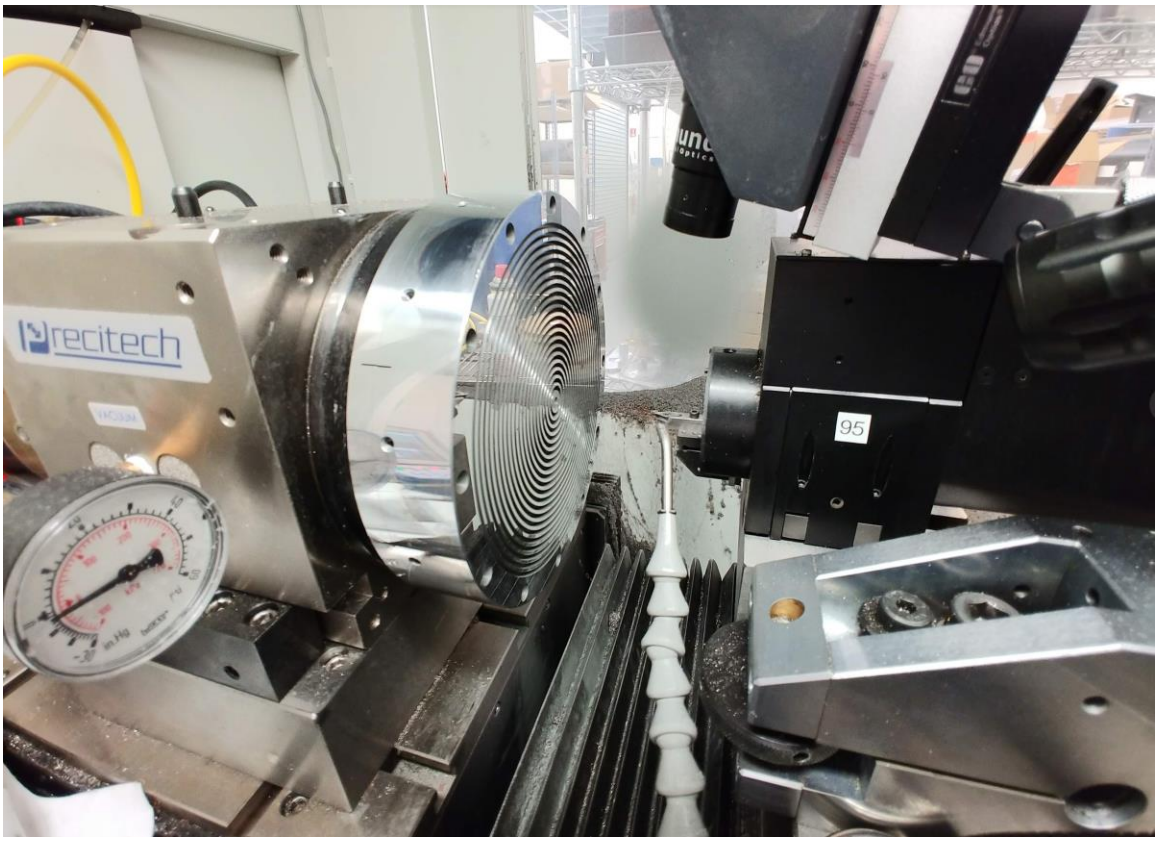

FIGURE 4: Machine & FTS Servo configuration

The recommended maximum relief angle limit of diamond lathe tools from several suppliers is 32°. If the negative slope exceeds the relief slope in FIGURE 2 position 1, the relief will contact the work and interfere with the cut. Therefore, a maximum tangential slope (φ_{const}) of 30° was chosen for the starburst pattern to account for imperfect diamond setup. An annulus width of 1mm was chosen to balance the need for a significant area to investigate with the desire to complete trial cuts in a reasonable timespan. Blend widths of 0.5mm were used on either side of the annulus to enter and exit the cuts.

Using 25.4mm diameter <111> germanium witness samples, the blend zone would extend from radius 12.7mm to 12.2mm (R_{max}), then the annulus from 12.2mm to 11.2mm, then the inner blend from 11.2mm to 10.7mm. To lessen the number of required cutting passes, 25um max amplitude (A_{max}) was targeted. Choosing a value of 300 for N resulted in an A_{max} of 23.5um and was used in the cuts.

Five samples were prepared with identical roughing parameters. Finish parameters were varied to observe any change in surface finish. Cutting parameters for each are given in

TABLE 1.

TABLE 1: Cutting Parameters

Sample	Stepover (um/rev)	Depth (um)	Count	Speed (mm/s)	Stepover (um/rev)	Depth (um)	Count	Speed (mm/s)
	Rough				Finish			
1	0.500	17	3	15	0.500	2	1	15
2	0.500	17	3	15	0.250	2	1	15
3	0.500	17	3	15	0.250	1	1	15
4	0.500	17	3	15	0.250	1	1	15
5	0.500	17	3	15	0.100	1	1	15

Speed is the constant tangential surface speed during the cut. The cut was performed in C axis mode and RPM was varied as a function of diamond radial position such that the surface speed was kept constant at any radius. This isn't possible to maintain as the diamond approaches the center as the RPM would approach infinity,

but the upper RPM limit occurs at a radius well inside the programmed annulus of the present cut and can be ignored.

Five new, natural single crystal, nominally identical diamonds were used, one per sample. Each diamond had a nominal nose radius of 200um, 0° rake angle, and 32° relief angle.

FIGURE 5: Annulus image contrasting the constant max slope region

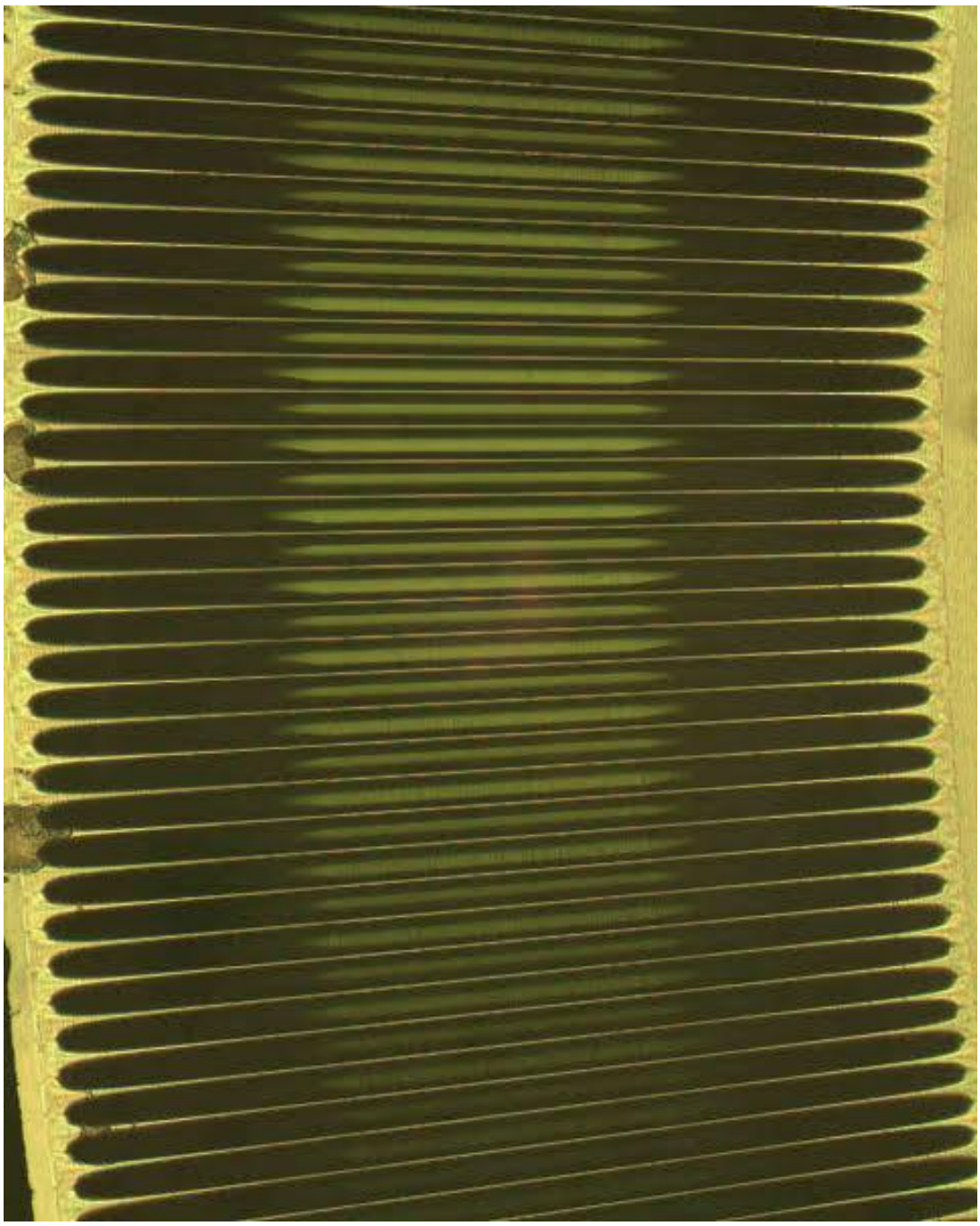

FIGURE 6: 2.5x Microscope image highlighting blend vs constant max slope regions

FIGURE 5 and FIGURE 6 show an example of how the starburst geometry appear in after completion. The central constant slope region is seen contrasted against the outer blend regions in both figures.

CHAPTER 3: MEASUREMENTS

Each of the five samples defined in

TABLE 1 were imaged with a SEM and measured on a Mahr profilometer. Areas of specific interest from manual optical microscope inspections on samples 3 and 4 were also measured on the NexView WLI.

Selected SEM images can be seen in the appendix from FIGURE 36 to FIGURE 45. The selected SEM images show approximately two cycles of the starburst wave in each image. Every image contains some evidence of a rougher texture on the descending slope (positive effective rake) than the ascending slope (negative effective rake).

During initial optical microscope inspections sample 3 appeared to have areas with almost no brittle fracture on descending slopes. These areas were indicated with a marker for further inspection with the NexView WLI. Sample 4 was also imaged to be used as a comparison.

Raw measurements were taken on the NexView using the 50X objective and 1X zoom with the assistance of Greg Caskey. Post processing analysis was performed in custom Matlab code to remove form and filter the data.

The analysis code removes surface form first by generating the ideal form from the starburst prescription in the general area the measurement was made using an initial guess for XY position. It then optimizes the form fit by optimizing XY position, tip, tilt, and yaw of the ideal form trying to minimize the RMS difference between the form fit and the data. This optimization uses a built-in Matlab function fmincon, a non-linear constrained multivariable solver.

After the solution converges, the resulting form-removed surface is filtered with a gaussian convolution filter with x and y cutoff wavelengths of 15um. This low-pass surface is subtracted from the form-removed surface to provide the high-pass results shown below.

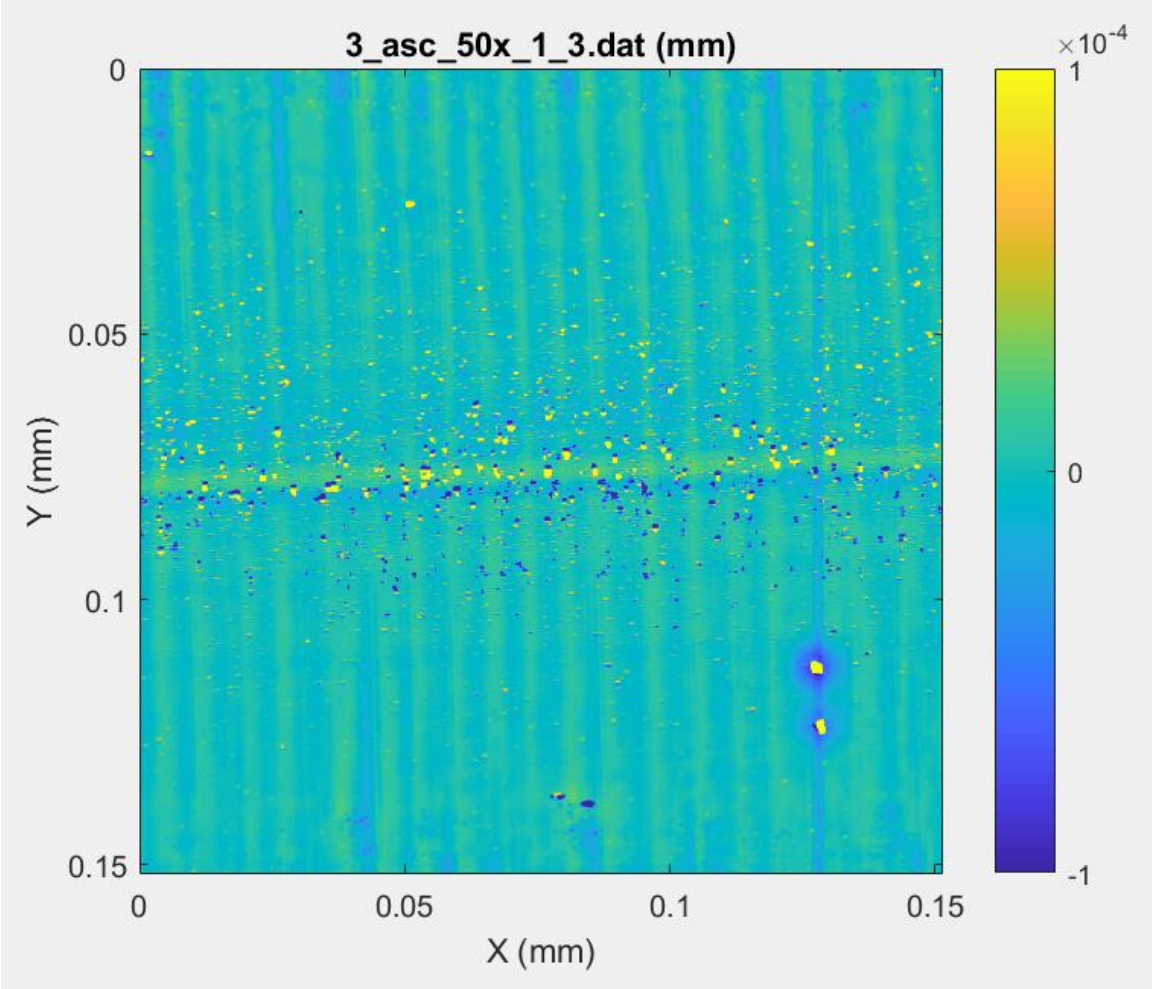

FIGURE 7: Sample 3 ascending slope

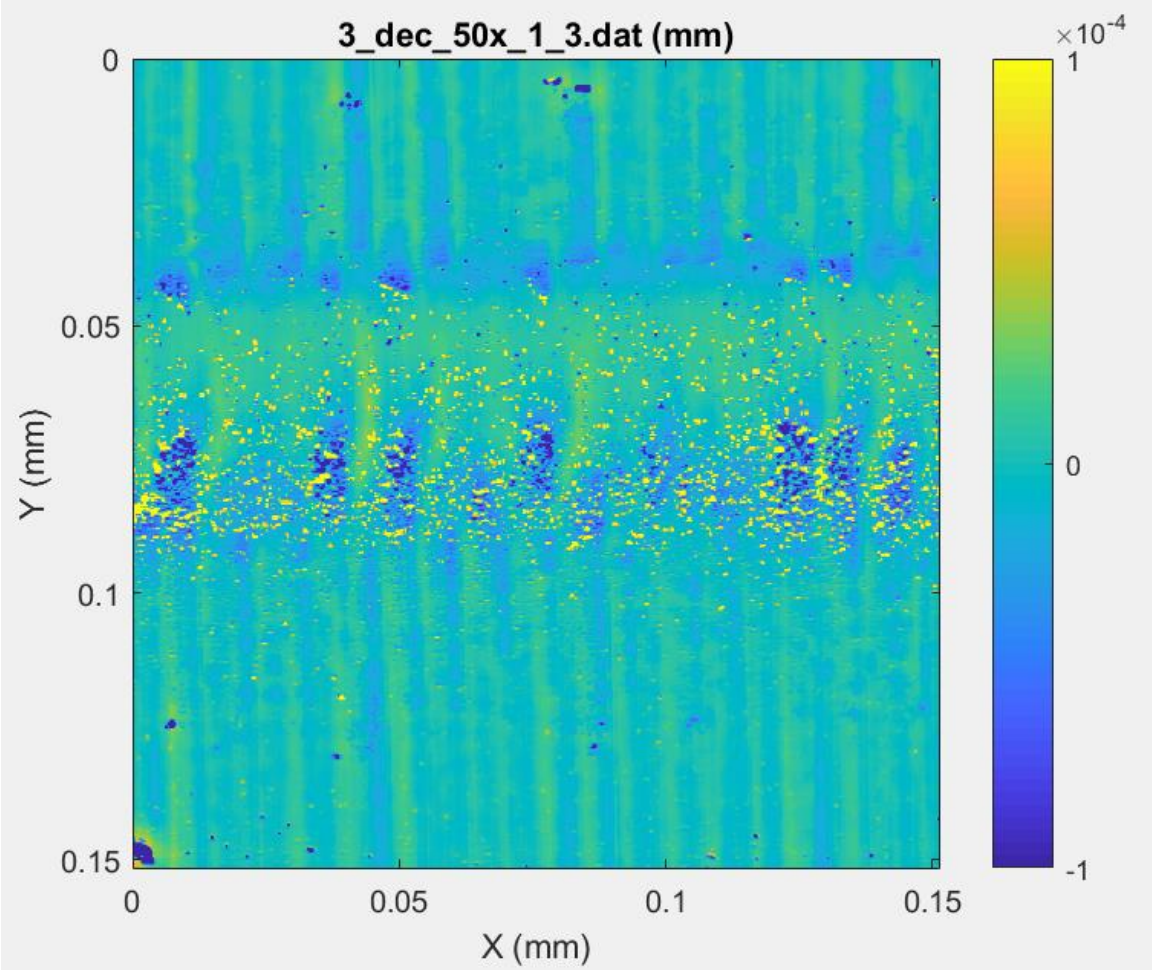

FIGURE 8: Sample 3 descending slope

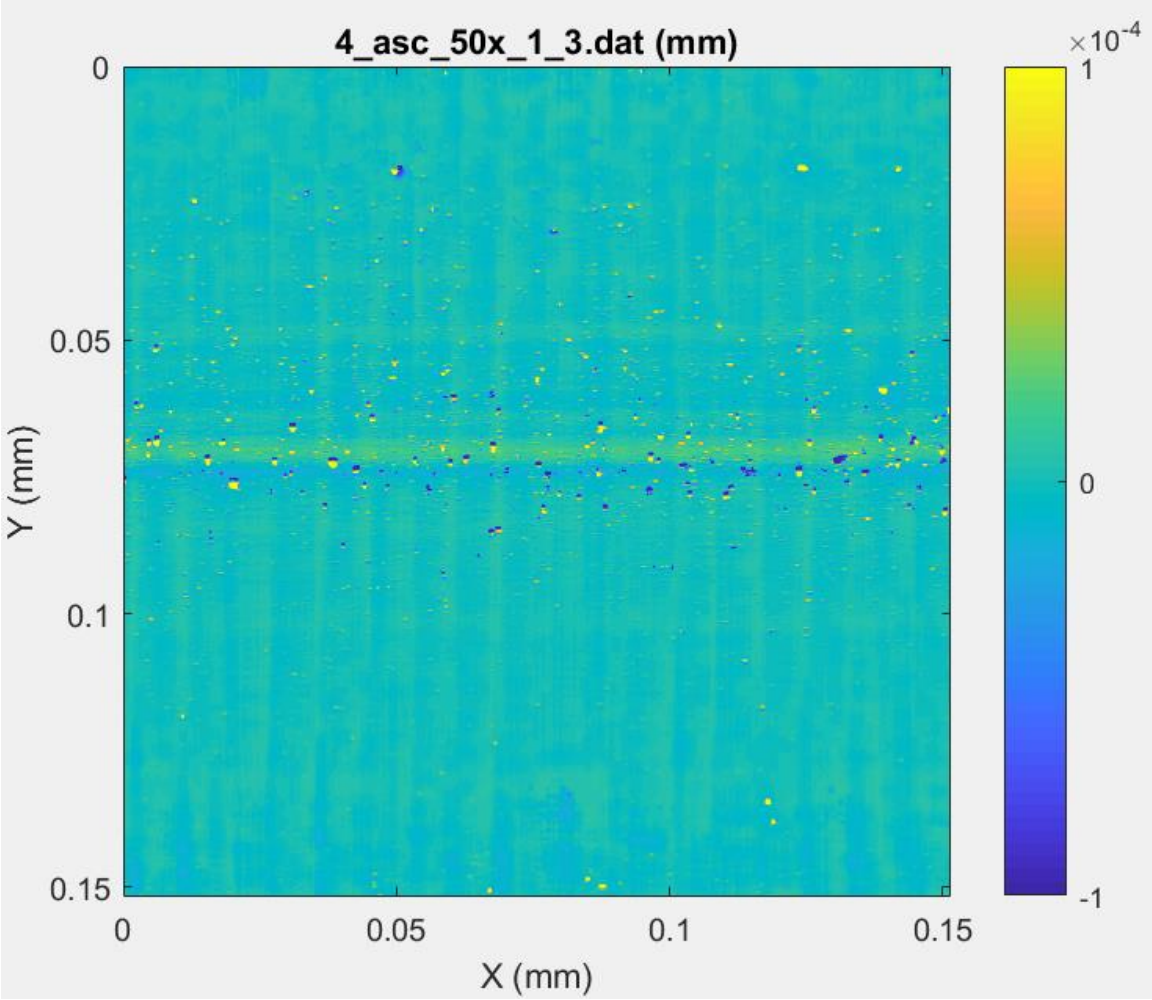

FIGURE 9: Sample 4 ascending slope

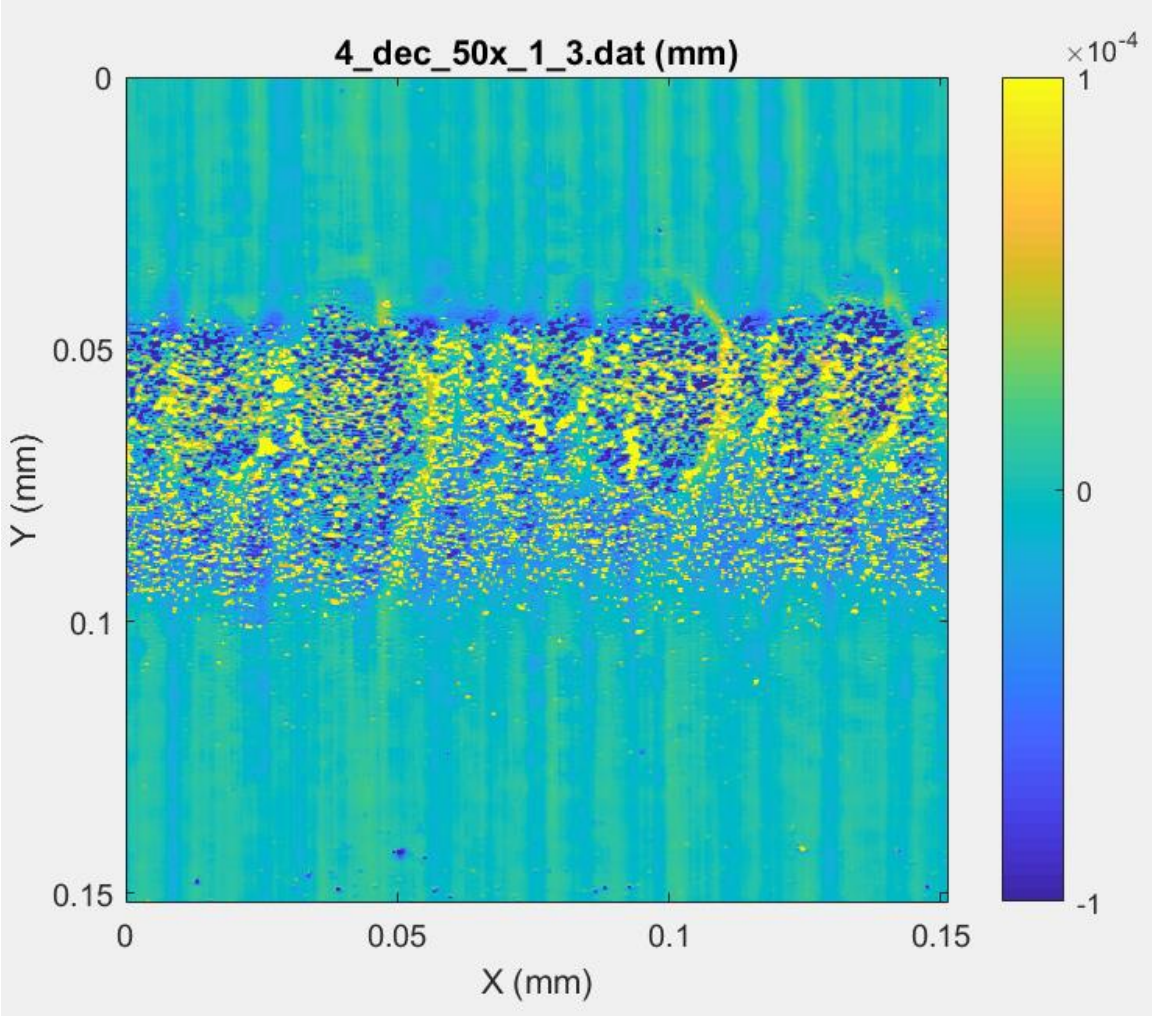

FIGURE 10: Sample 4 descending slope

As can be seen in FIGURE 7 and FIGURE 9, samples 3 and 4 have similar qualitative textures on the ascending slopes where the rake is negative. From FIGURE 8 and FIGURE 10 it can be seen that sample 3 and 4 have significantly different textures on the descending slope where the rake is positive. Sample 3's descending slope texture resembles the typical ascending slope on both samples which represent ductile cutting. Sample 4's descending slope has a much rougher texture from the brittle fracture at the max slope portion.

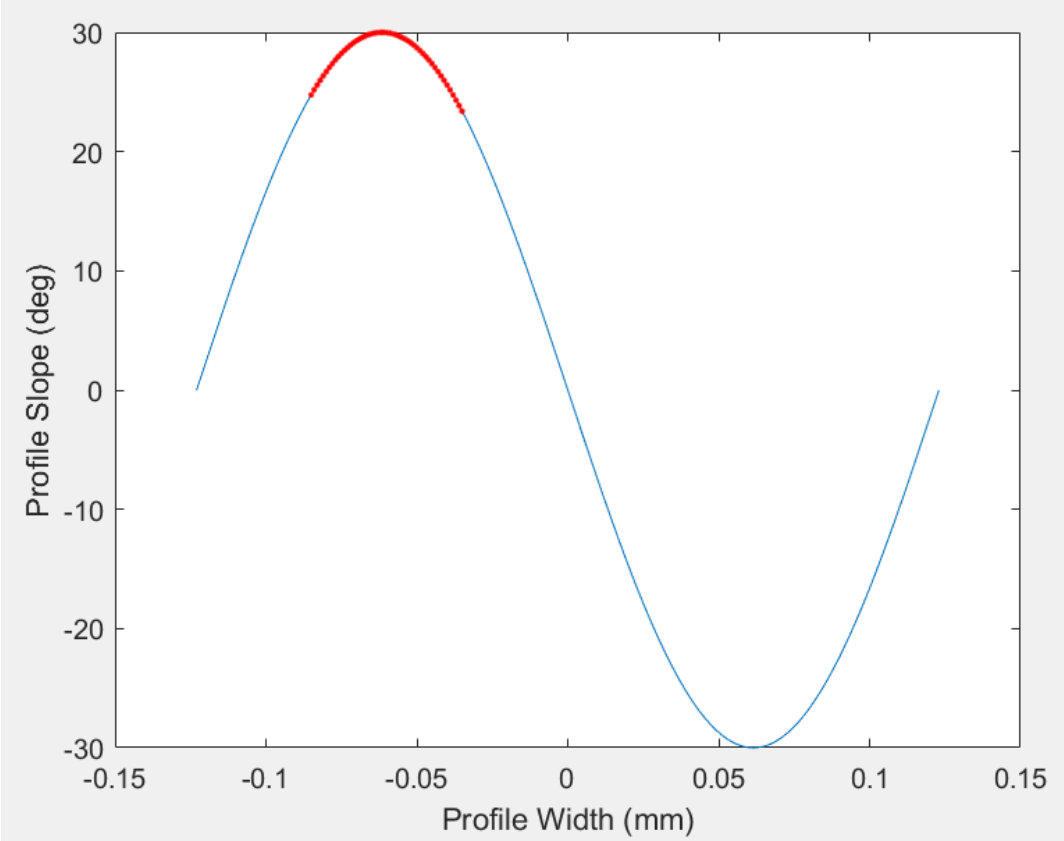

FIGURE 11: Profile slope plot; Central 50um of descending slope highlighted in red

Each disturbed region in the descending slope figures appears to be about 50um in width. This would correspond with positive tool slopes in the range of 25-30° as can be seen in FIGURE 11.

The WLI measurements are useful to give insight into the morphology of the fracturing, but the lack of automation made 100% sampling of each ridge impractical. The profilometer measurements filled this measurement gap.

Profilometer measurements were taken on the Mahr profilometer with a 2um radius stylus. Data was taken in rotary stage mode with the assistance of Greg Caskey. Each sample was centered on the rotary stage of the profilometer and measured

clockwise rotating the stage 400° so there would be 40° of overlap. Precise centering of the sample was not necessary as the 1mm width of the constant max slope region of the annulus provided a sufficiently large allowable region for the stylus.

Post processing analysis of the data was again performed in custom Matlab code to first segment the profile into each wave cycle, remove form, and filter.

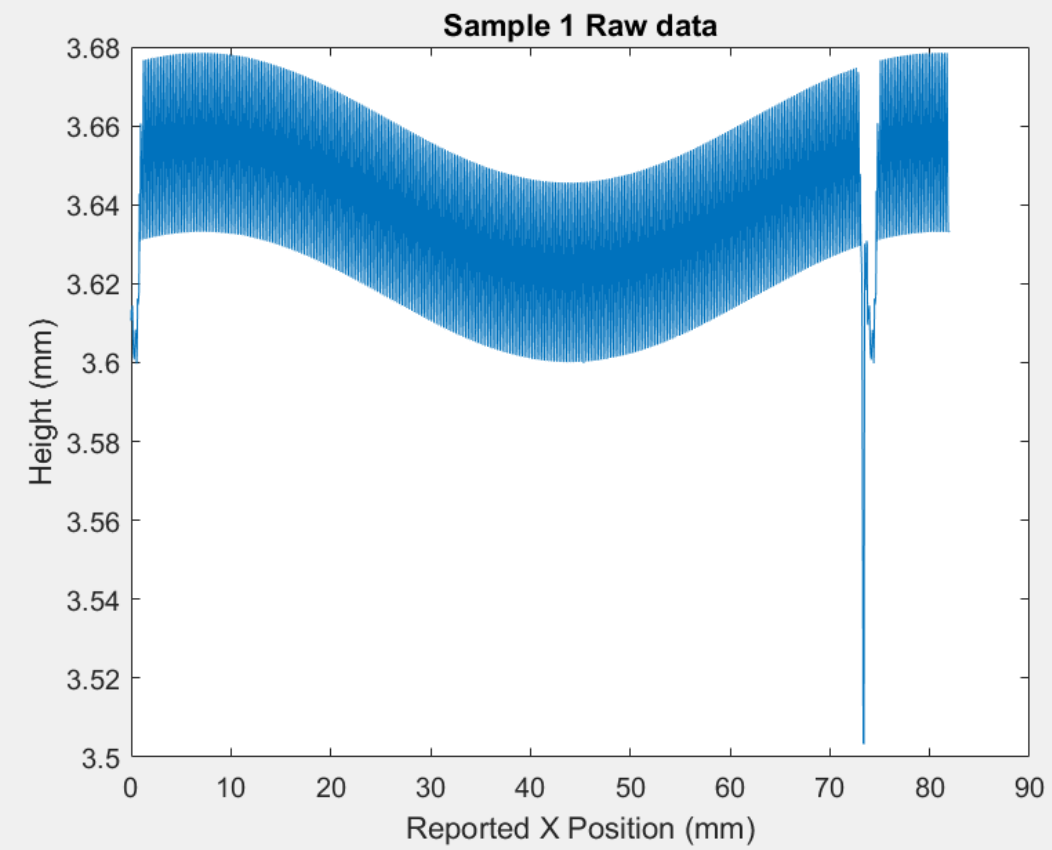

FIGURE 12: Sample 1 Raw data

The raw data output from the profilometer requires significant post processing. First, in FIGURE 12 it can be seen there is a low frequency error occurring likely due to wedge in the measurement fixture. Second, there are isolated regions with junk data that need to be excluded. Third, while not apparent in FIGURE 12, the period of the sine

wave changes slightly throughout the measurement. This could be explained by a decentered sample being measured.

The code first isolates the locations of individual waves by generating an ideal wave and walking it along the raw data. At each position, the RMS difference between the ideal wave and raw data are calculated and saved.

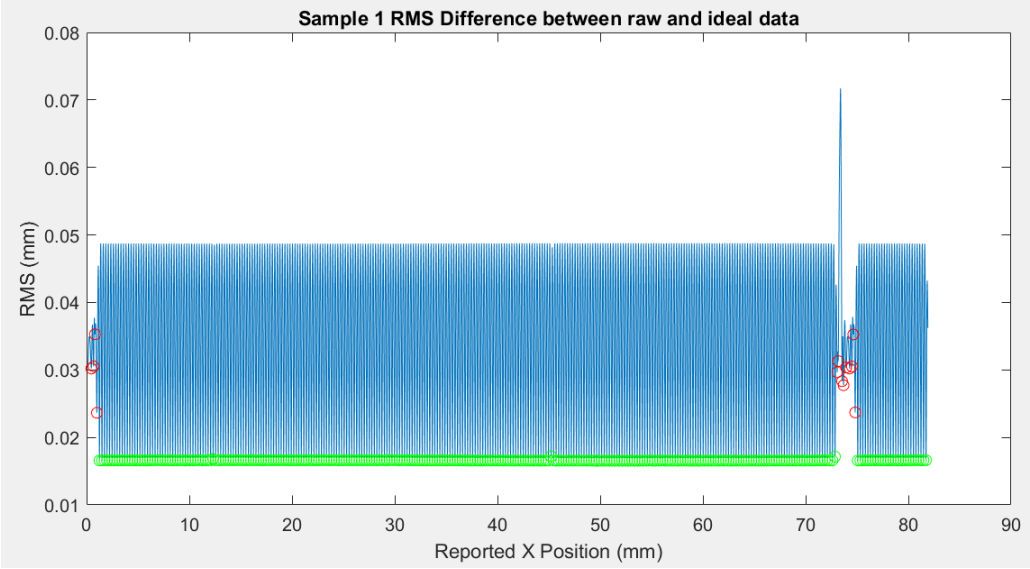

FIGURE 13: Sample 1 RMS Difference between raw and ideal data

In FIGURE 13 the RMS difference between ideal and raw data at each position is shown. Local minima were isolated as potential segment center positions shown in green. Local minima with RMS values above 20um were excluded, shown in red. The segments centered on each valid local minimum were isolated and had the ideal form removed. These form-removed segments were then bandpass filtered using a robust gaussian filter based on one demonstrated in (Muralikrishnan & Raja, 2008) with period limits of 15um and 2um. The 2um high frequency cutoff was based on the radius of the stylus used.

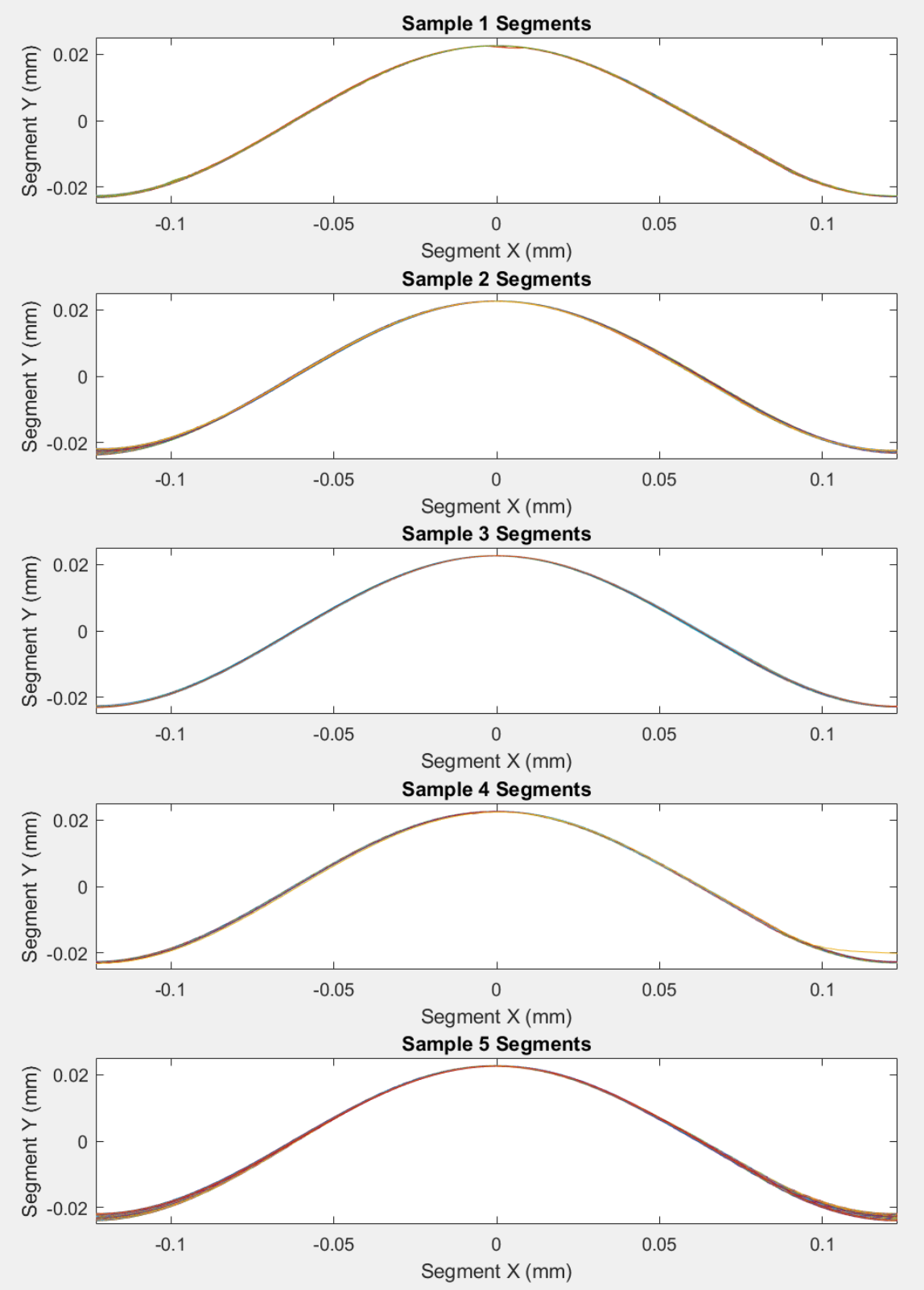

FIGURE 14: Overlaid segments for samples 1-5

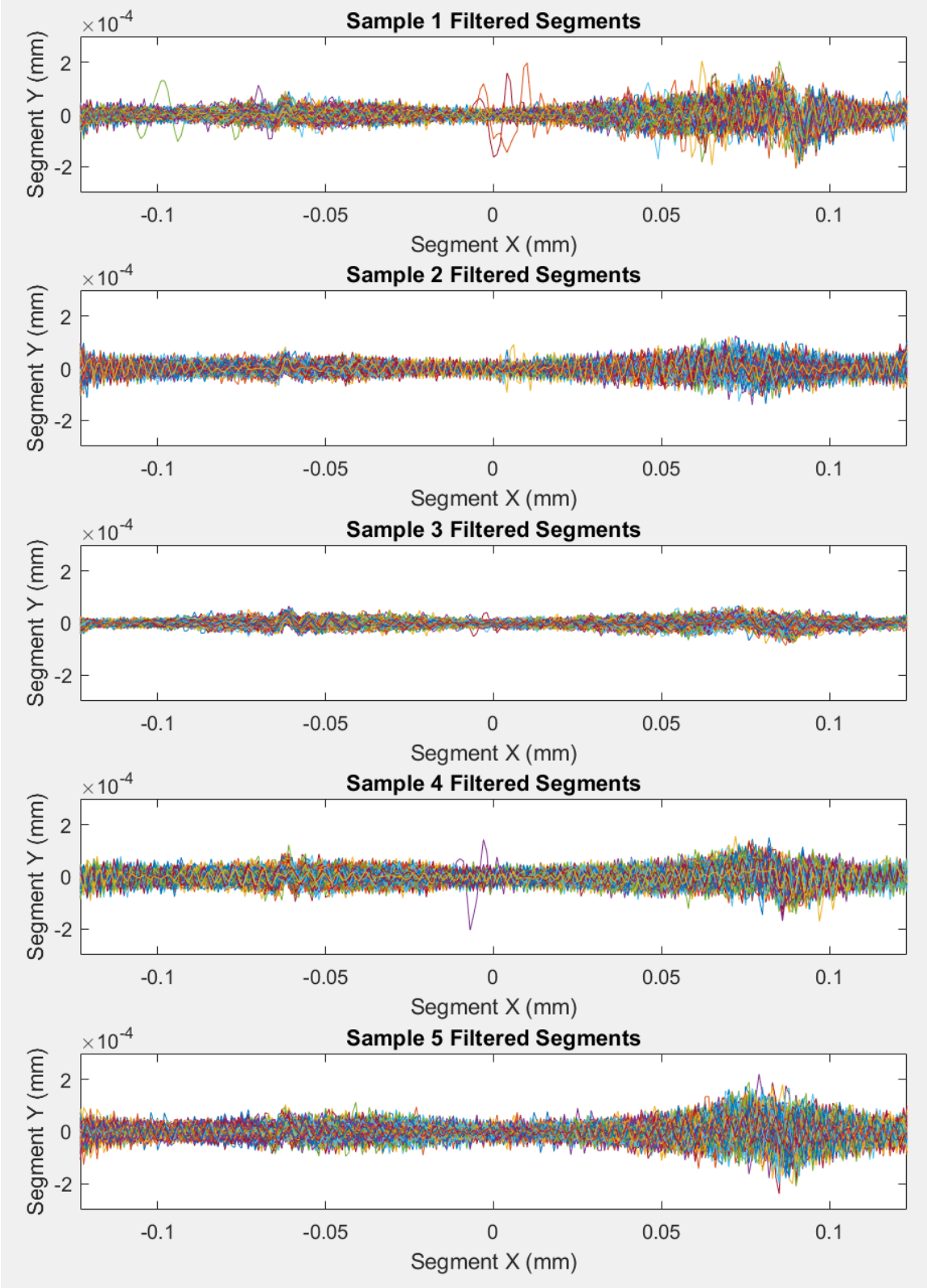

FIGURE 15: Filtered segments from samples 1-5

Isolated segments can be seen overlaid in FIGURE 14. FIGURE 15 shows those same segments with form removed and filtered as described above. Because the diamond tool was moving in the same direction as the stylus, the negative rake region is on the left side of the plot, and the positive rake region is on the right. In each case, the positive rake slope is much rougher than the negative rake slope. Sample 3 again shows the least amount of roughness on the positive slope.

CHAPTER 4: INDUSTRIAL APPLICATION

Based on the findings of the previous tests with 0° rake diamonds, work began at FLIR attempting to use negative conical rake (chamfer) diamonds to achieve ductile cutting on both ascending and descending slopes of a 'starburst' test part and then applying that capability to cutting convex spheres that simulate lenses. Little emphasis was placed on quantifying the amount of brittle fracture. Simple microscope and stereoscope observations were used to identify the presence or absence of fractured areas.

For initial testing, a negative conical rake diamond was used. The diamond had a nominal conical relief of 32°, nominal conical rake of -30°, and 500um nose radius. All tests cuts were done in <111> germanium.

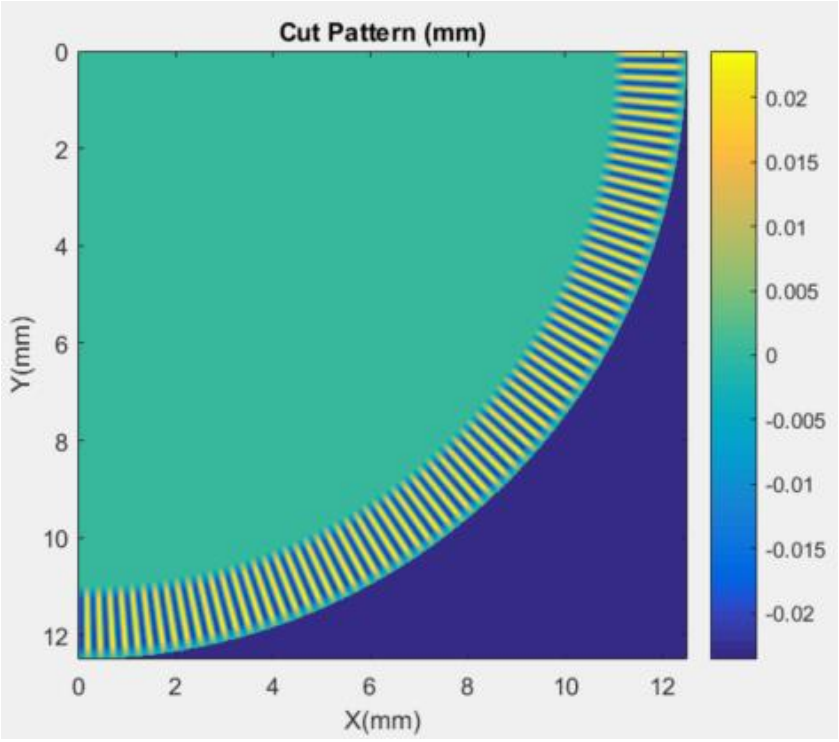

FIGURE 16: Simulation of FLIR Test 01

The first test was cut in a witness sample 25.4mm diameter, 2mm thickness. As shown in FIGURE 16, the outer blend zone of the starburst extended from the outer edge to 12.25mm radius. The constant slope region anulus was located from outer radius 12.25mm to inner radius 11.25mm. The inner blend extended from 11.25mm radius to 10.75mm radius. There were 300 sine waves in one rotation of the anulus with a maximum PV or 47.15um and a maximum slope of 30°. There were 2 rough cuts, 20um depth of cut each with a 5um infeed per rev. There was a single finish cut, 20um deep with 1um infeed per rev. All sine wave tests used a 15mm/s surface speed.

At completion of the cut, macroscopic fracturing of the surface was observed prior to dismounting the sample from the chuck. It was decided to recut this surface with less aggressive parameters without any further observation.

Test 02 was then overcut on Test 01 with identical nominal geometry. Two finish cuts were done each with 5um depth of cut, and 1um infeed per rev.

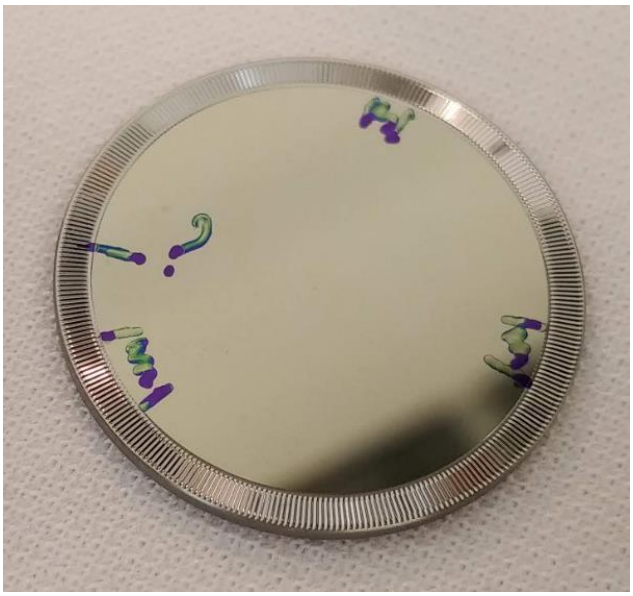

FIGURE 17: Completed FLIR Test 02

The completed part as seen in FIGURE 17 was annotated with areas of interest during inspection. The 3 indicated ranges were identified to have minimal brittle fracture on the descending slope. The areas, roughly separated by 120°, seem to agree with the expectation that there would exist 3 crystal orientations with maximum likelihood of ductile cutting. No brittle fracture was observed on the ascending slopes.

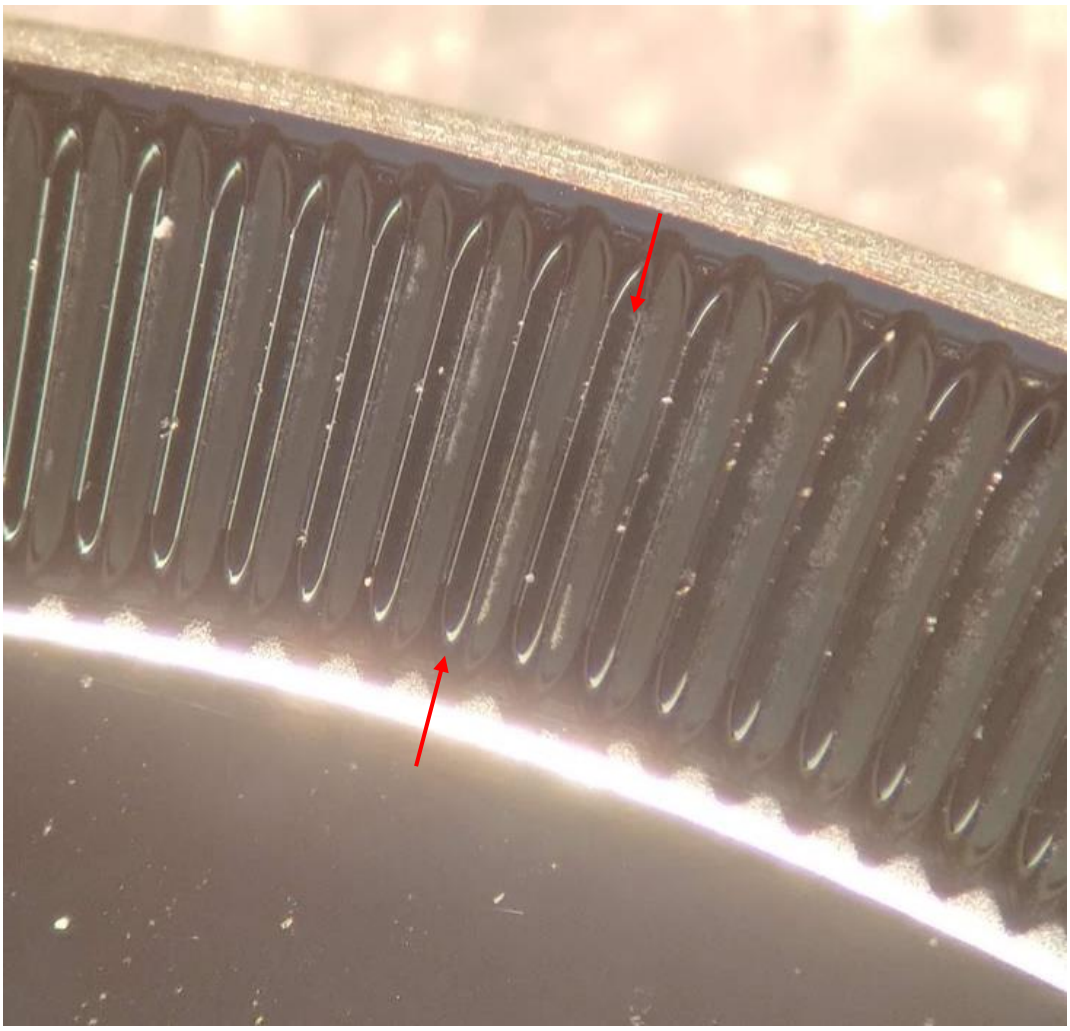

FIGURE 18: FLIR Test 02 Stereoscope Image

FIGURE 18 shows one area of minimal fracture. Red arrows indicate waves with incomplete fracture along descending edge.

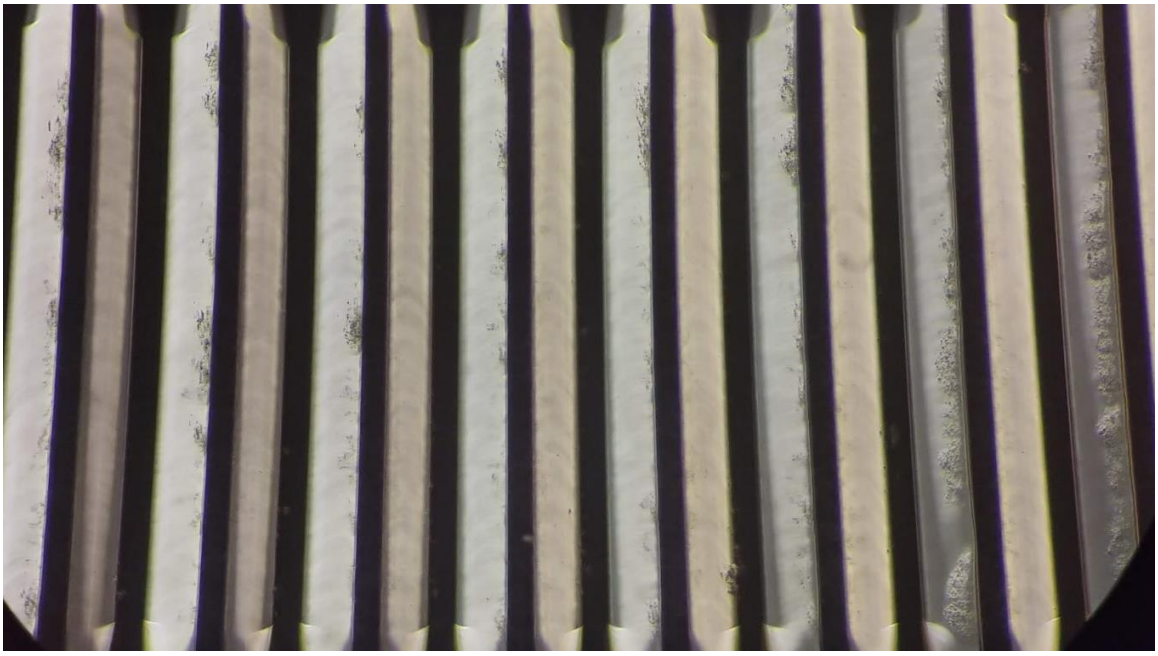

FIGURE 19: FLIR Test 02 Microscope Darkfield Image

FIGURE 19 shows microscope darkfield images taken in the region of the part with the least amount of fracture reveal isolated areas where fracture persists. The relatively small observable area prompted a change to a higher sag starburst configuration with fewer oscillations.

Test 03 was cut in a different witness sample from tests 1 & 2. For this test, the annulus region was kept identical to tests 1 & 2 but number of oscillations was reduced from 300 to 100 and sag increased from 47.15um to 141.451um to maintain a constant max slope of 30°. The rough cut was done over 30 passes of 5um depth of cut with a 5um infeed per rev. The finish cut was done in one pass with 5um depth of cut and 1um infeed per rev.

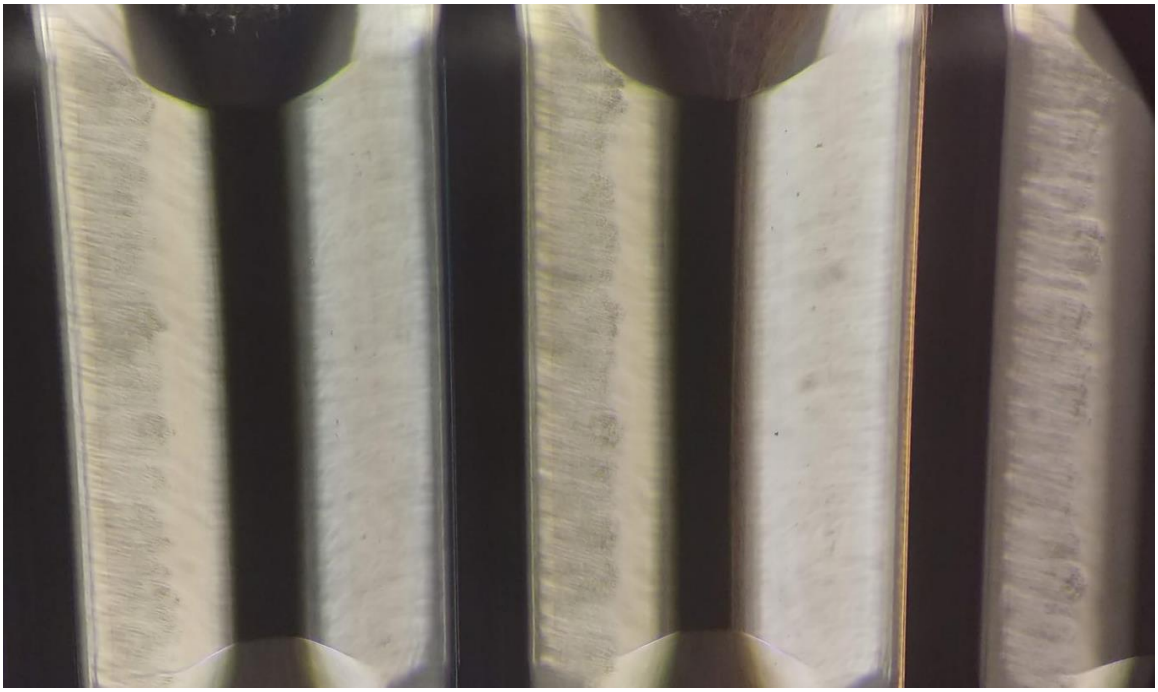

FIGURE 20: FLIR Test 03 Microscope Darkfield Image

This resulted in consistent brittle fracture on the descending slope over the entire anulus. FIGURE 20 shows an example of the fracture. One interesting aspect of this higher sag feature is it seems to show fracture developing at near max slope and then persisting into regions of lower slope. It was quickly concluded that less aggressive cutting parameters were necessary.

Test 04 was cut on the same part as Test 03, but on an anulus inside of the anulus of Test 03. This preserved the Test 03 features and allowed for direct comparison of Test 03 features to Test 04 features for a given crystal orientation. The outer radius of the annulus was 10.75mm and inner radius was 9.75mm. Relative positions of the anulus can be seen in FIGURE 21.

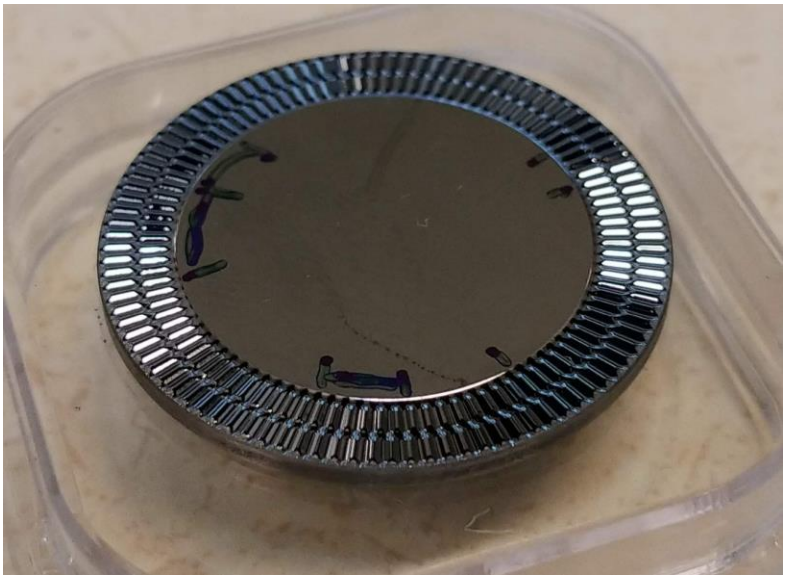

FIGURE 21: FLIR Test 04 Completed Sample

Oscillations per rev were kept at 100 per rev, but to keep maximum slope at 30° it was necessary to reduce sag to 124.13um. The rough cut was done over 30 passes, 5um depth of cut and 5um infeed per rev. The finish cut was a single pass, 5um depth of cut and 0.2um infeed per rev.

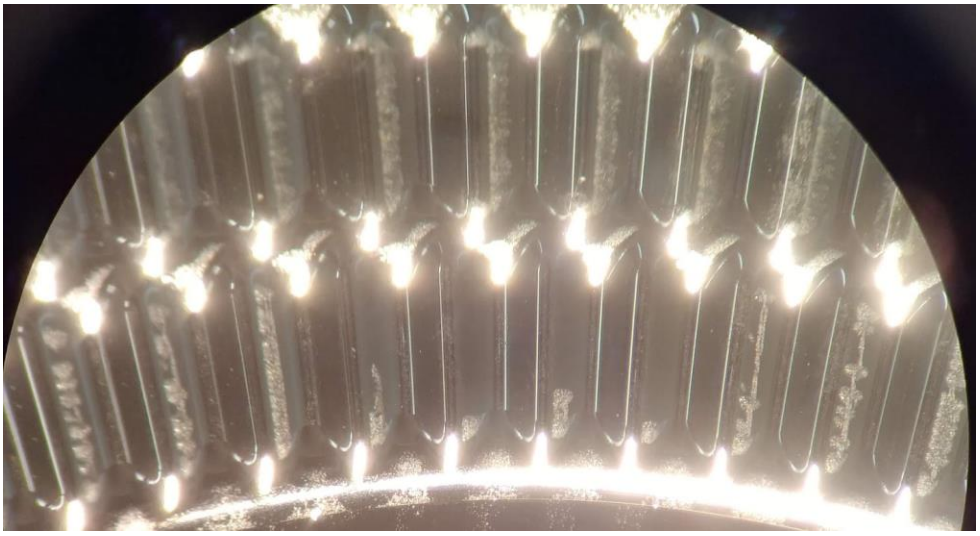

FIGURE 22: FLIR Test 04 Location 01 Stereoscope Image

FIGURE 22 shows a portion of the Test 03 anulus in the top half of the image and the Test 04 anulus in the bottom half of the image. There was significant improvement in ductile cutting performance in the Test 04 anulus. This test also had an unusual fracture signature in the form of linear features combined with larger ‘spots’ of fracture.

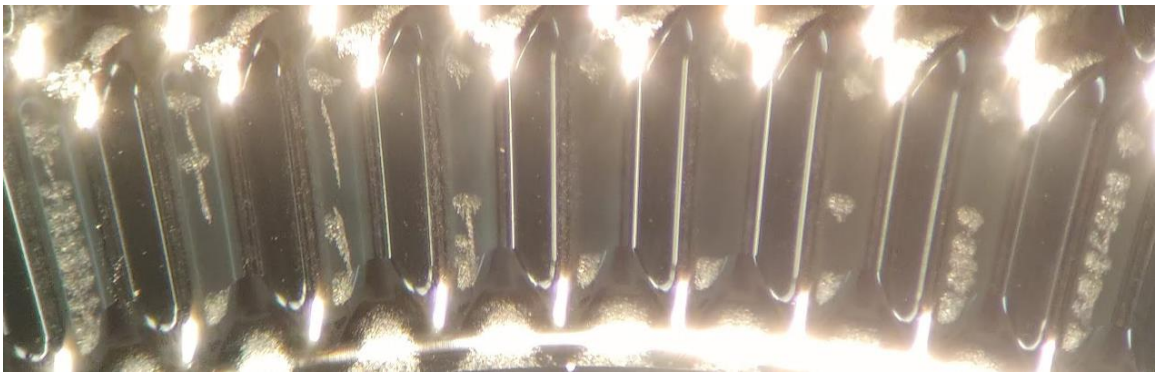

FIGURE 23: FLIR Test 04 Location 02 Stereoscope Image

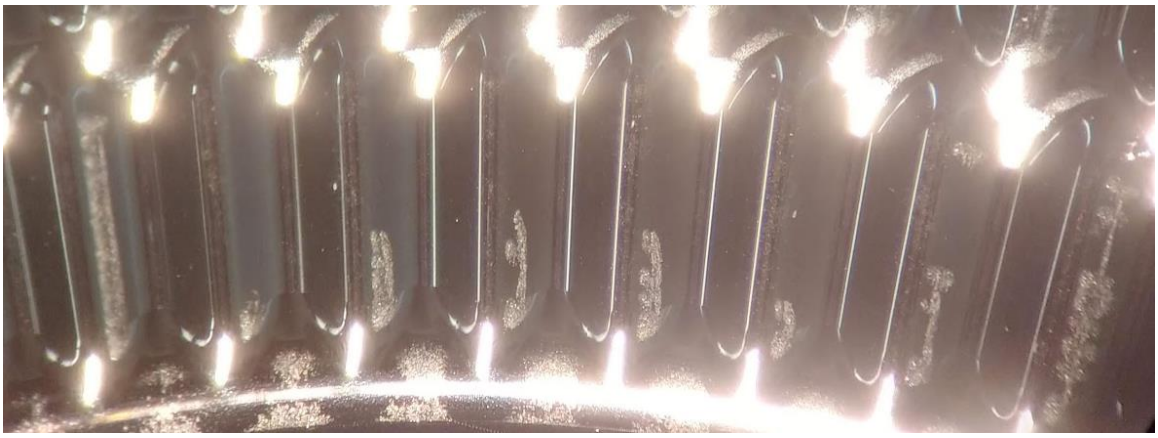

FIGURE 24: FLIR Test 04 Location 03 Stereoscope Image

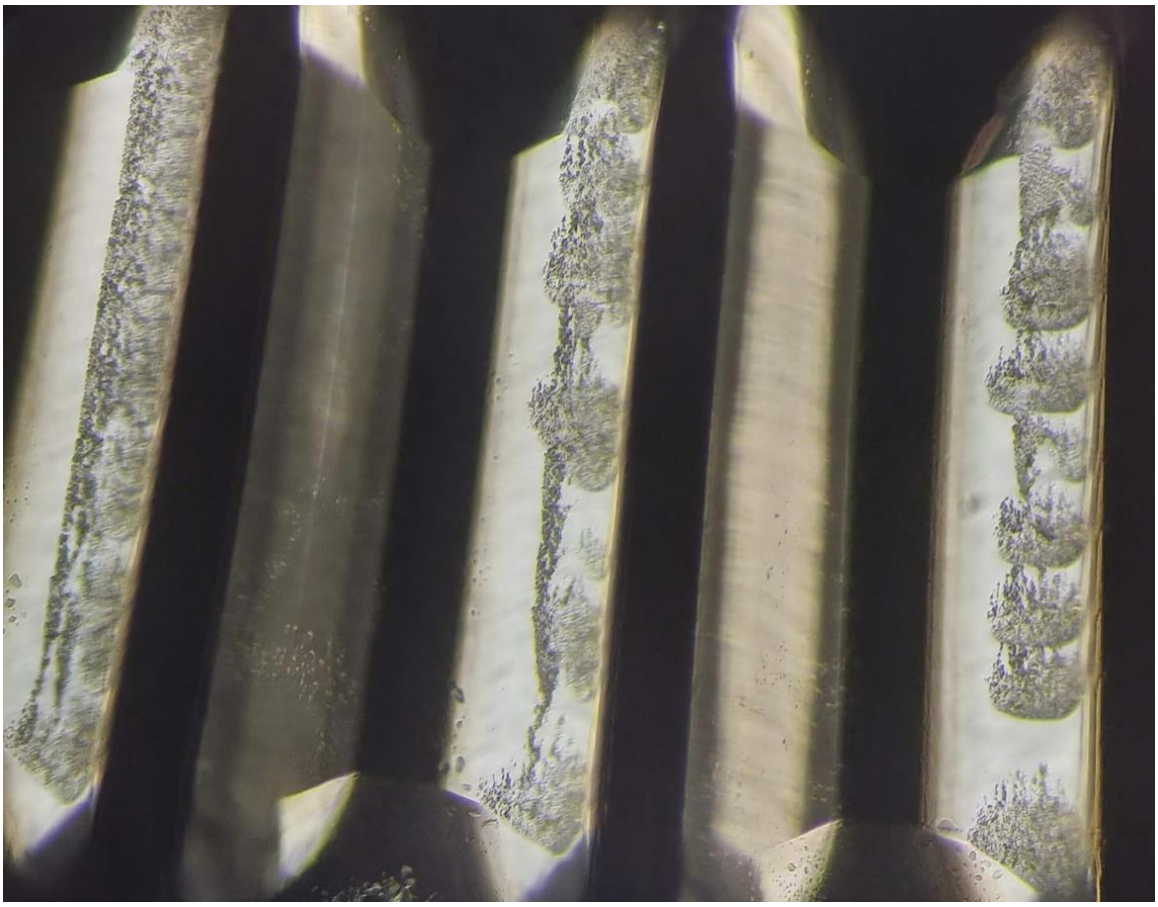

FIGURE 25: FLIR Test 04 Location 04 Microscope Darkfield Image

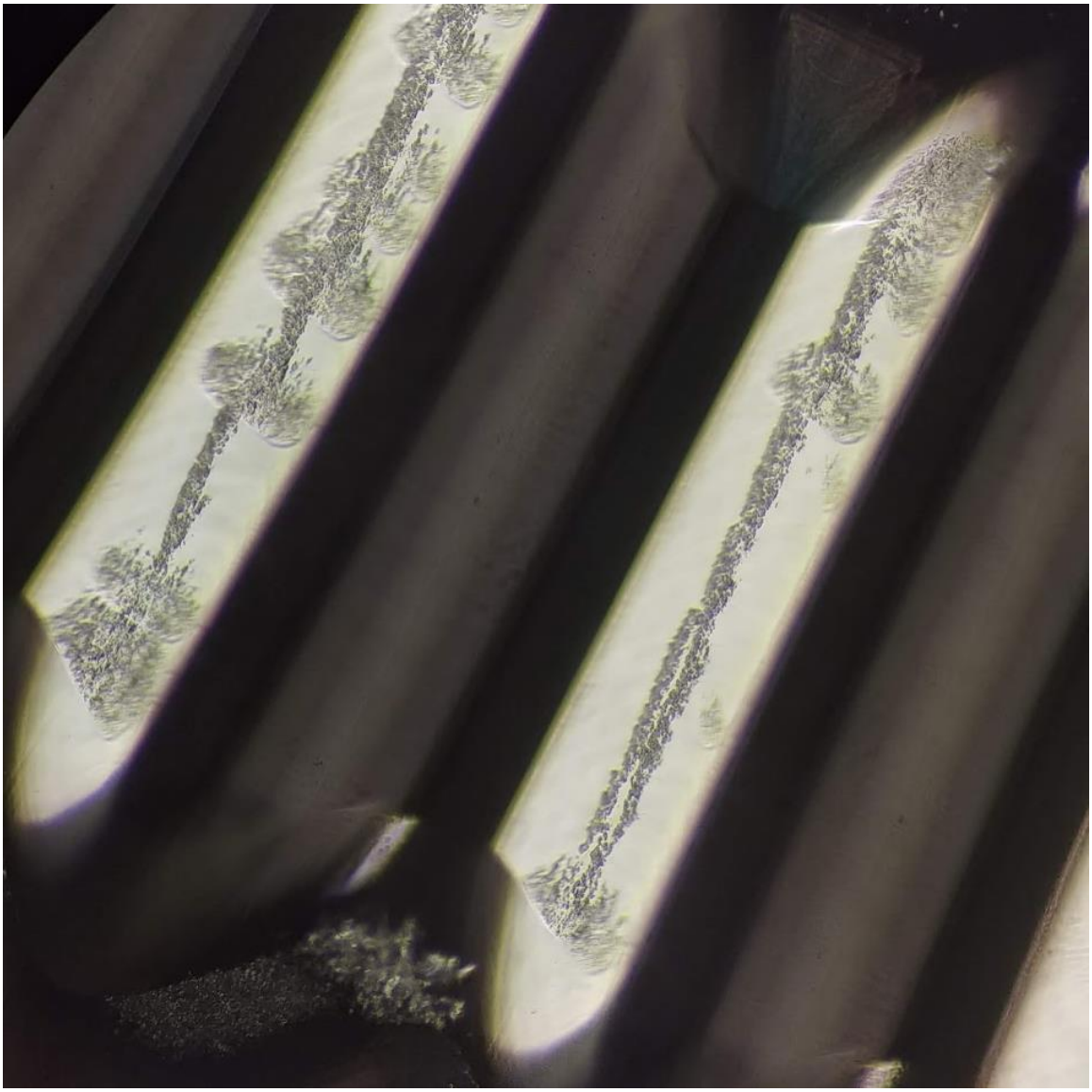

FIGURE 26: FLIR Test 04 Location 01(partial) Microscope Darkfield Image

FIGURE 23, FIGURE 24, FIGURE 25, and FIGURE 26 show additional examples of this unusual fracture signature.

At the completion of Test 04, it was concluded that further decreasing the infeed per rev may reduce brittle fracture but would not result in a workable process due to very long cut times. It was decided to try similar diamonds with a more negative rake.

Two additional diamonds were purchased identical to the first diamond except the rake angles were -35° and -40° respectively. It was also decided to test these new diamonds by directly cutting a hex packed convex spherical lens array. The prescription of the lens was chosen to have a max slope of 30°. The edge of the lens transitioned to the surrounding field by a concave 600um RoC blend that was tangent to both the lens and the field. When paired with the blend, the apex of the lens was 1mm above the field.

The array was first roughed in with the -30° diamond. It was thought that while the larger negative rakes may help maintain ductile cutting on the descending slopes, it may cause unnecessarily large compressive forces on the ascending slopes during aggressive roughing and cause chipping.

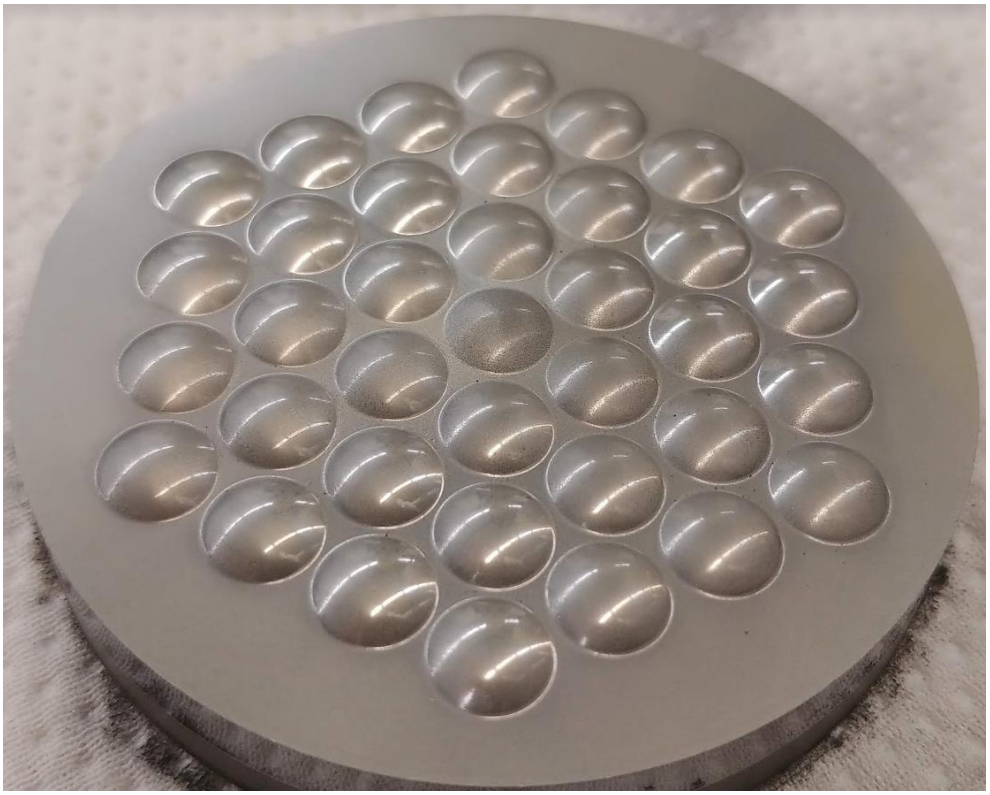

FIGURE 27: FLIR Hex Packed Array, Roughed

In FIGURE 27 the completed roughed sample can be seen to have no macroscopic chipping. The rough was completed using 50 passes with 20um depth of cut, 20um infeed per rev, 60mm/s surface speed. The cut was completed in about 35 hours.

For the first finish test, the -35° was used. The finish was completed with a single pass, 10um depth of cut, 2um infeed per rev, and 60mm/s surface speed. The cut took about 7 hours.

FIGURE 28: FLIR Hex Packed Array 1st Finish Cut

The completed array can be seen in FIGURE 28. Only slight brittle fracture apparent to the naked eye in the form of spoke fracture in the center lens.

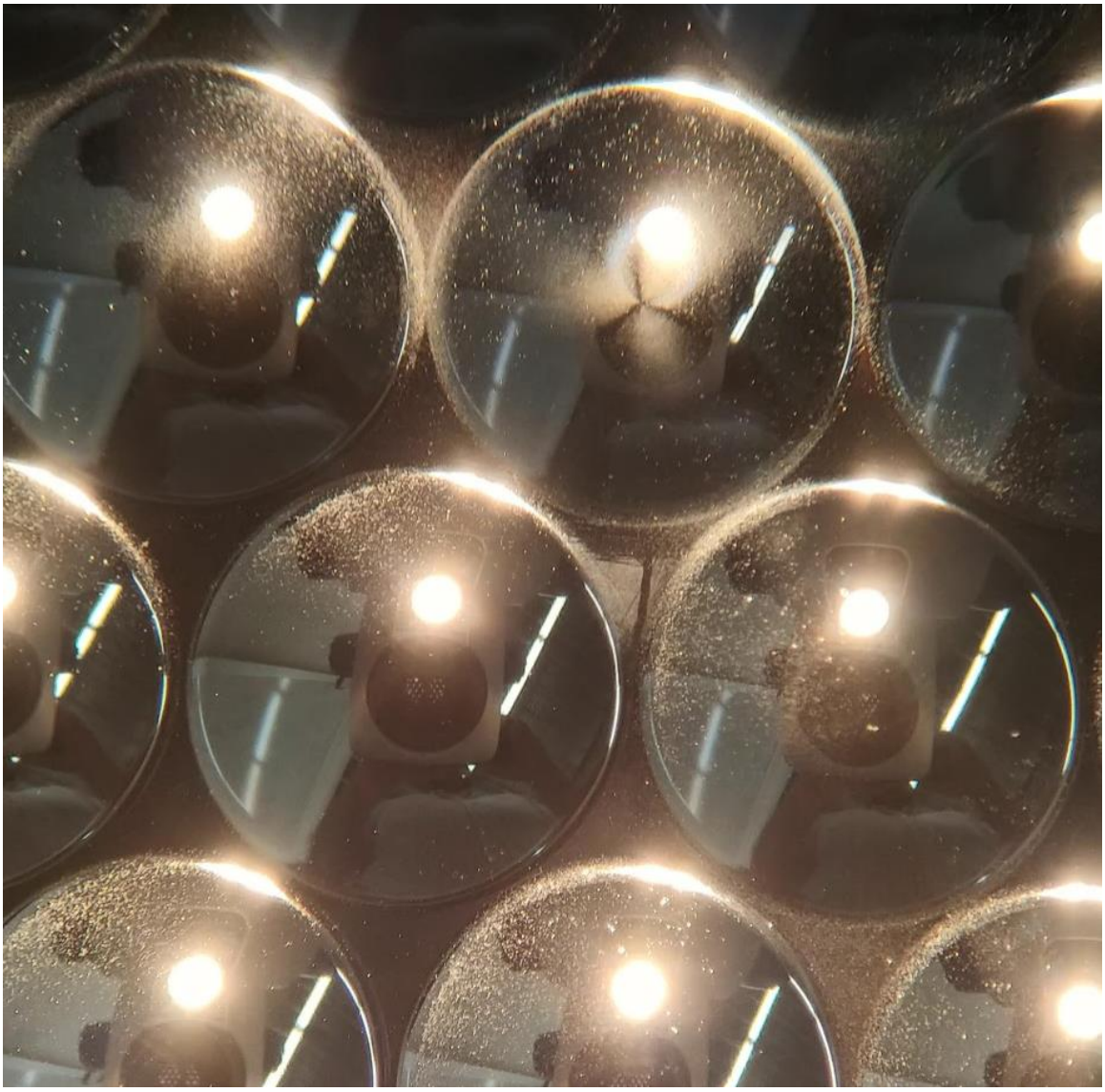

FIGURE 29: FLIR Hex Packed Array 1st Finish Cut, Central Lenses

In FIGURE 29 the spoke fracture can be seen in the central lens, and ascending slope fracture can be seen in the surrounding lenses.

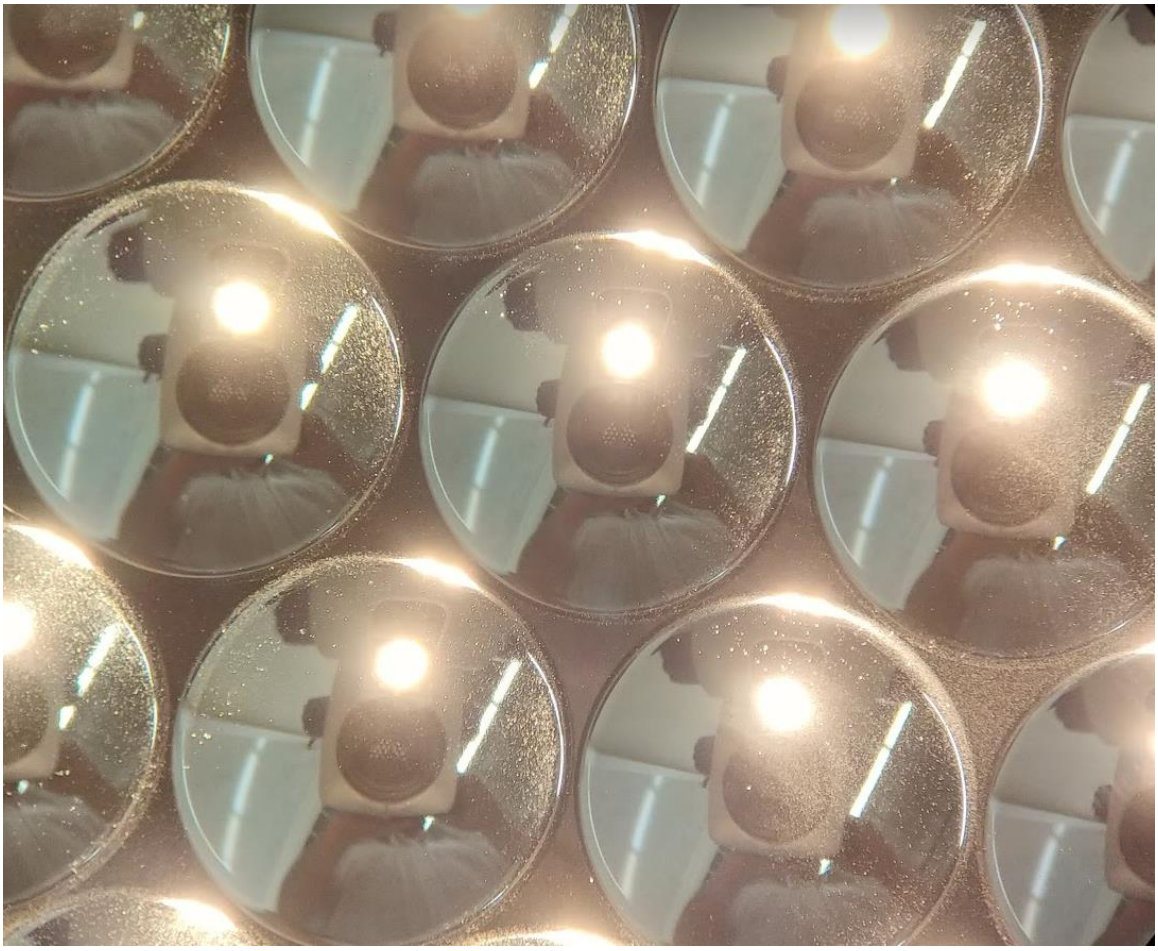

FIGURE 30: FLIR Hex Packed Array 1st Finish Cut, Outer Lenses Above Center

FIGURE 30 shows the ascending slope fracture extends out to the edge of the array. Based on these results, it was decided to recut over this sample with a smaller infeed per rev of 1um.

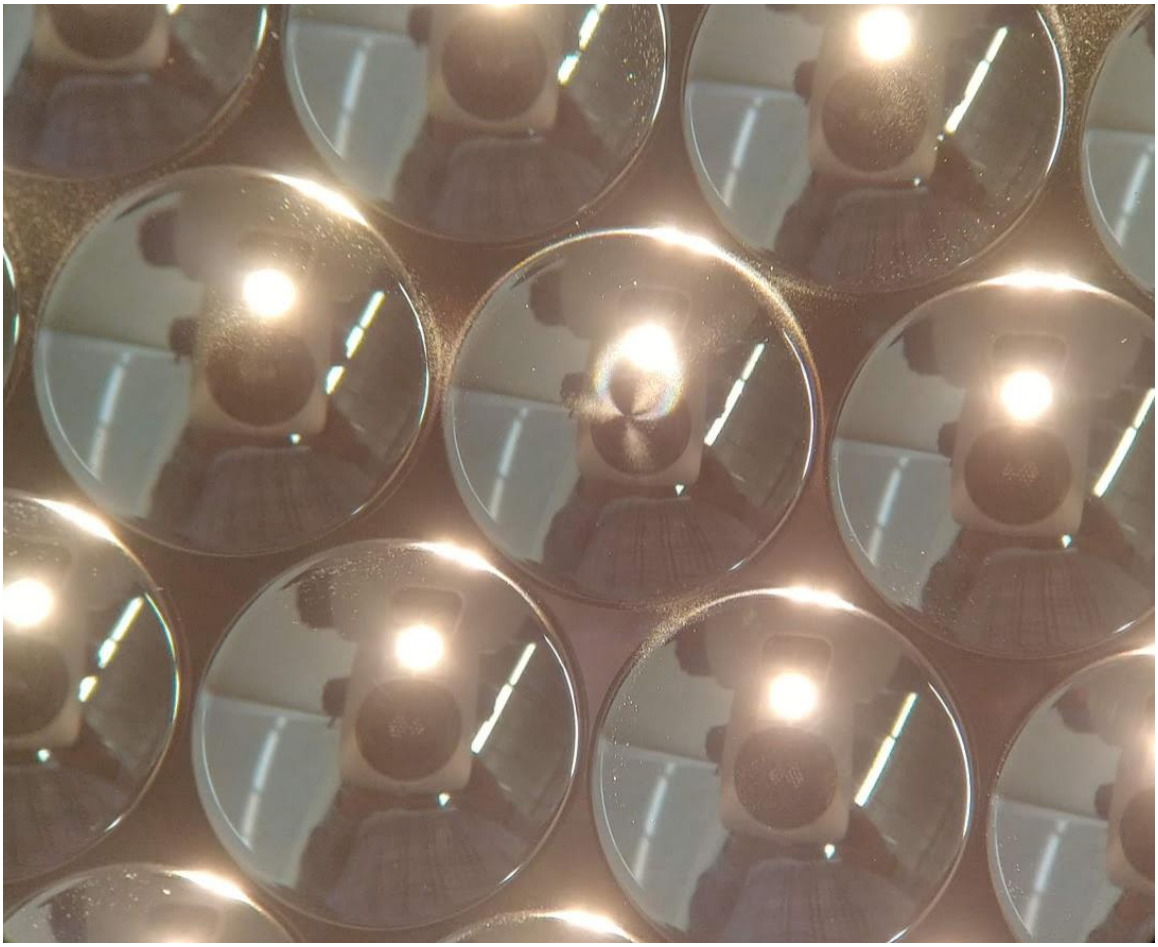

FIGURE 31: FLIR Hex Packed Array 2nd Finish Cut, Central Lenses

FIGURE 31 shows the results of the 2nd finish cut with smaller infeed per rev of 1um. This cut took about 14 hours to complete. The central spoke is much less pronounced. Interestingly, while there is some evidence of brittle fracture in the surrounding lenses, the extension of the spoke fracture is most apparent in the surrounding field. This doesn't agree with the notion that the most likely area for brittle fracture to occur would be on the descending slopes of the lenses where the effective rake angle would be least negative.

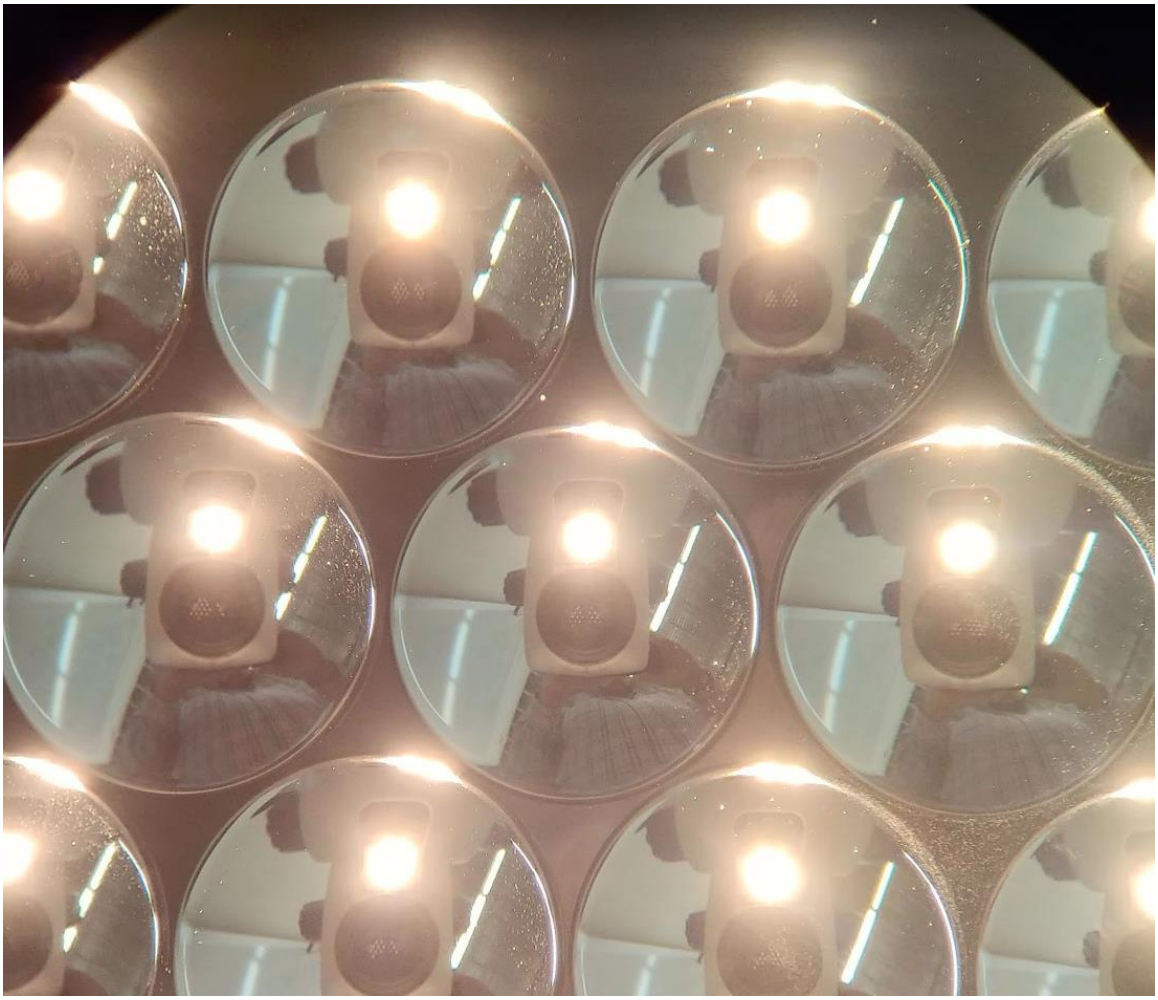

FIGURE 32: FLIR Hex Packed Array 2nd Finish Cut, Outer Lenses Above Center

FIGURE 32 shows this same effect of modest brittle fracture on the outer lenses extends out to the edge of the array.

For the 3rd finish cut test on the hex packed array, the infeed per rev was again halved from 1um in the 2nd finish cut to 0.5um in the 3rd finish cut. The 3rd finish cut took about 28 hours to complete.

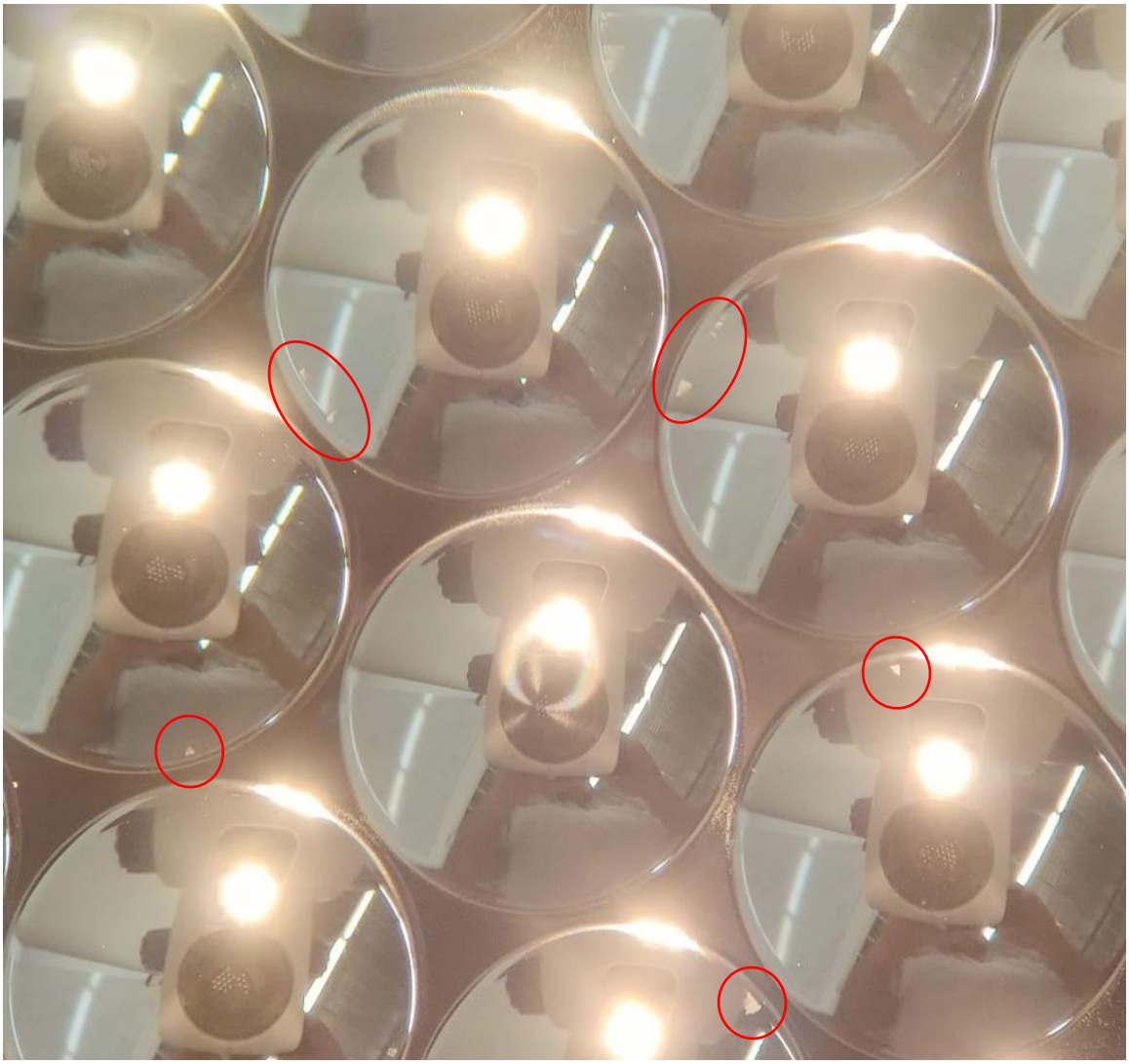

FIGURE 33: FLIR Hex Packed Array 3rd Finish Cut, Central Lenses

FIGURE 33 shows the results of the central lenses after the 3rd finish cut. The central spoke fracture area is again significantly reduced. The surrounding lenses are largely free of fracture except for isolated spots, circled in red, near the edge of the lens on the descending slope near the area of minimum effective rake angle as expected. However, the presence of spoke fracture in the central lens and extending out in the surrounding field is unexpected.

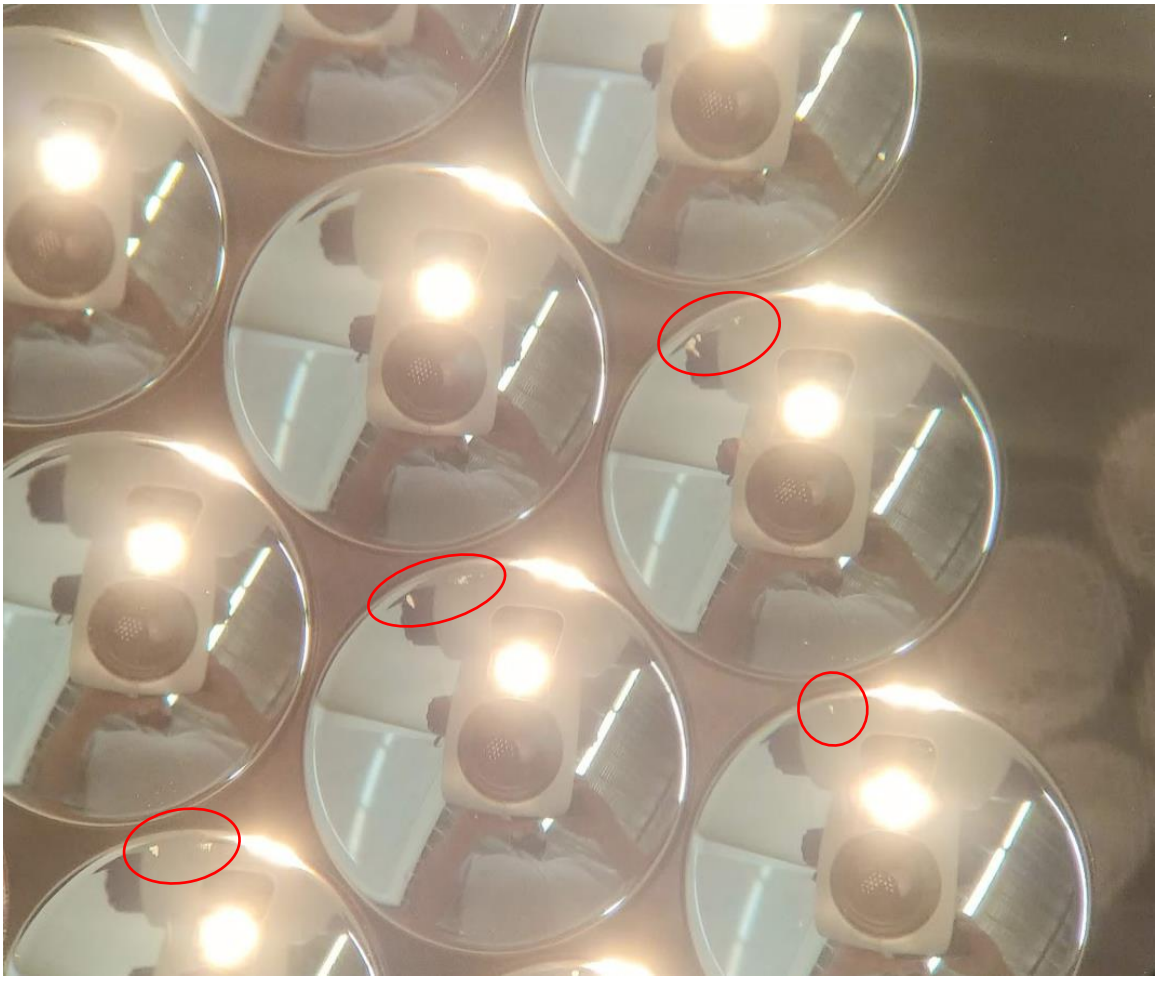

FIGURE 34: FLIR Hex Packed Array 3rd Finish Cut, Outer Lenses Right of Center

FIGURE 34 shows the same effect extends out from the central area to the edge of the array.

Next, roughing was started on a second germanium part to test out the -40° finish cut performance. Roughing was again done with the -30° diamond and cutting parameters kept the same except for the surface speed was increased from 60mm/s to 90mm/s. This reduced the roughing time from about 35 hours to about 28 hours. The change in roughing speed did not produce any macroscopic chipping.

The first finish cut with the -40° diamond was run with identical parameters to the 3rd finish cut with the -35° diamond.

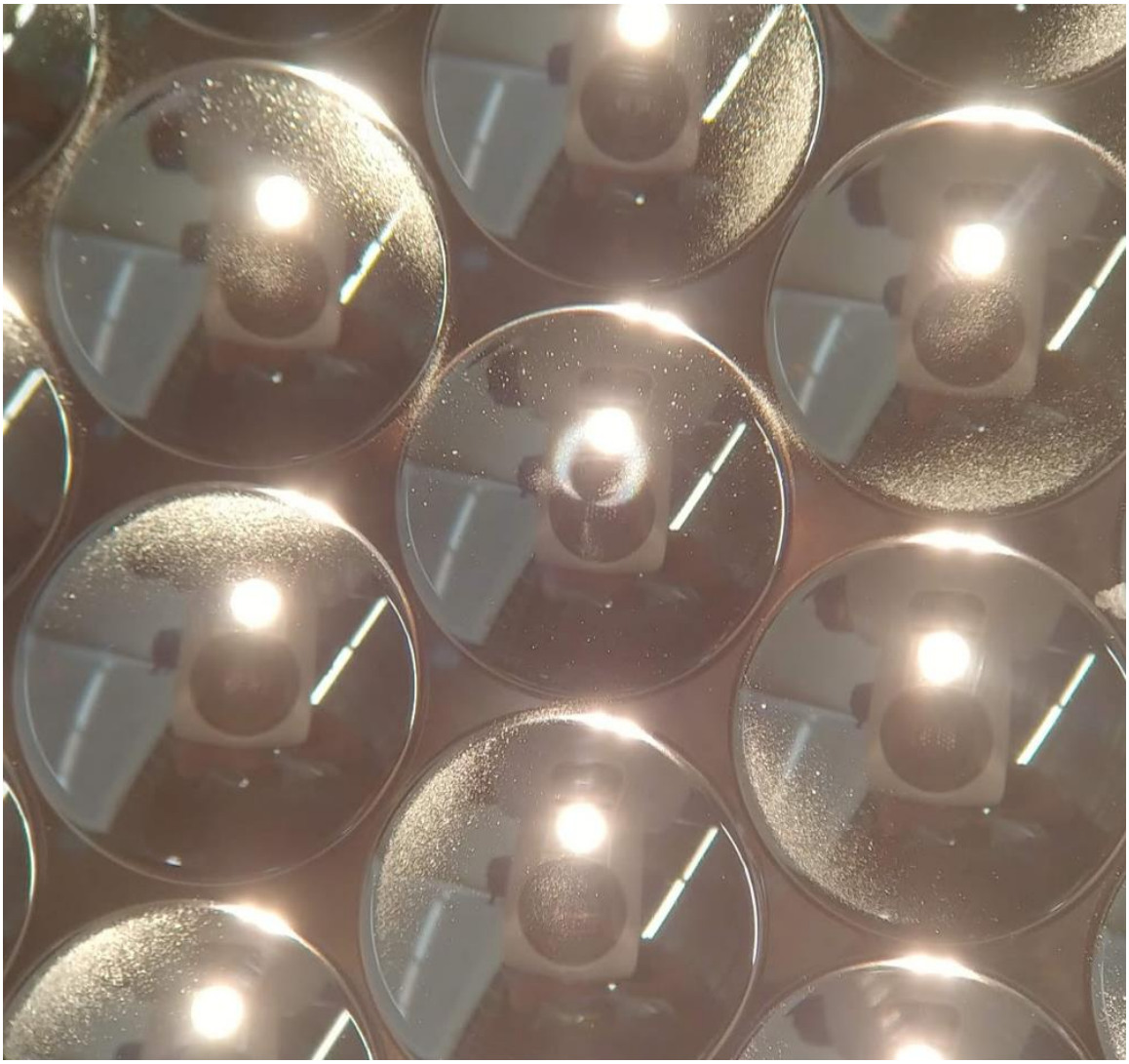

FIGURE 35: FLIR 2nd Hex Packed Array 1st Finish Cut, Central Lenses

FIGURE 35 shows that while the -40° diamond the same or slightly improved central spoke area and descending slopes without fracture, it had significant ascending slope fracture on every lens. This seems to indicate the exceeding of some compressive force limit on the ascending slopes where the effective rake angle is -75°.

CHAPTER 5: CONCLUSION

This thesis has shown that the novel process of using starburst geometry cuts is superior to direct lens array cuts for the purposes of optimizing cutting parameters and diamond selection for variable rake cutting processes. The starburst geometry allows for high slopes, minimal radial gradients, and many features to be cut in a limited area with minimal cut time and minimal sag. Starburst geometry provides a line of equivalent gradients along each wave which provides a means of comparison while lenses have unique gradients at each point.

Roughness metrology of starburst samples was demonstrated in several forms. Fracture patterns were observed with SEM, SWLI, profilometer, and manual microscope observations and measurements. In each case, the fracture patterns agreed with the expectation that descending slopes would have increased roughness.

In the context of developing a fast, efficient process for optimizing cutting parameters, the SEM images were arguably the least useful. SEM ownership is less ubiquitous, and operation is much less convenient than some of the other options. It would also be very time consuming to collect data on large numbers of waves. It does provide superior fidelity of fracture morphology, but this is likely not needed in an industrial setting that places more importance on removing fracture than characterizing it.

The SWLI measurements suffer some of the same disadvantages of the SEM. It would be very time consuming to collect and analyze data on many waves. Analysis of the fracture morphology can be done but simple detection of the fracture is likely

sufficient for industrial applications. While it would be desirable to assign local slope to specific areas of fracture, measurement tilt removal is nontrivial. A datum would need to be established across many waves on a part requiring a large area to be measured and stitched together. The tilt of that datum would need to be removed from the local measurement of each wave for the measured local slope to be accurate. A better approach may be to put an upper bound on the possible tilt error of the measured area and determine if this error would contribute in a significant way.

Profilometer measurements proved to be the best option for mass data collection across all waves of a sample. With this data, analysis can be performed to map roughness of waves vs azimuth position on the sample that may reveal 'spoke' regions of waves that are all brittle or ductile. It may also be the best option to assign absolute slope to measured points due to the available full-azimuth dataset. The disadvantages of the profilometer approach lie in convenience, tool availability, and difficulty of analysis. Profilometers that can measure straight line profiles are quite common and many of these tools include a rotary table as a positioning axis. However, this measurement requires the rotary axis to move as a measurement axis. Profilometers with this capability are quite uncommon.

Manual microscope observations were the most convenient and most useful of the tested options especially in an industrial setting. The disadvantages of microscope observations include the uncertainty of observing fracture on high slopes, and subjectivity when identifying fracture roughness vs debris or lighting effects.

Significant practical knowledge was gained in the industrial application of the process at FLIR. Appropriate SEM and profile measurements were not readily available, and SWLI measurements had great difficulty at the highest slopes. It was during this time that microscope observations proved sufficient to identify presence or absence of fracture areas.

Higher sag, lower frequency starbursts were also tested in the industrial setting under the hypothesis that fracture initiation may be dynamic, depending on the duration a diamond spends cutting at a rake that would cause fracture under steady state conditions. The higher sag features also displayed a larger area for more convenient observation of ascending and descending slopes. When cutting these features with identical parameters to the lower sag features, the descending slopes on the larger sag features displayed larger bands of roughness. The larger area also aided the observation of these fracture bands being asymmetric on the descending slope. It appears that once fracture has begun at a high slope, it does not stop until the slope decreases well below the slope at which it started. The disadvantage of the higher sag starburst is that it occupies a larger segment of the full part azimuth. Occupying a small segment can be desirable for investigating crystal orientation dependence. With cutting parameters that create narrow spokes of ductile-only or brittle-only areas, it would be desirable to have many waves in the narrow area to provide some resolution in theta within the spoke. A single, large wave that occupies an entire spoke or is larger than a spoke would be a poor feature to represent the fracture within the spoke.

Further work needs to be done to evaluate the extent of subsurface damage that would not be detected in the inspections and measurements described in this thesis. Further work also needs to be done to identify the cause of the unexpected fracturing in the central lens and field of the hex packed array. These areas, cut with the nominal negative rake of the diamonds, should be less likely to fracture than the descending slopes of the surrounding lenses which appear free of fracture. It could be that the resolved forces while cutting on the downward slope of a lens are more favorable to ductile machining than cutting on the normal face of the <111> crystal which occurs when cutting the field and central lens. It could also be an effect of machining speed. The surface speed in every test is much slower than typical on-axis cuts. Additionally, while lateral surface speed is kept constant, absolute speed including the z actuation speed of the servo is fastest at the highest slopes. The surface speed at a 30° slope can be up to 15.5% faster than the lateral speed. This could be tested by increasing the nominal speed to see if this effect changes.

It may also be possible to learn more by turning multiple annuli of flats with varying speeds inside the starburst annulus. This could create an in situ reference for spoke intensity and alignment to any spokes that may be observed in the starburst waves.

REFERENCES

Blackley, W. S., & Scattergood, R. O. (1991). Ductile-regime machining model for diamond turning of brittle materials. *Precision Engineering*, 95-103.

Blake, P. N., & Scattergood, R. O. (1990). Ductile-Regime Machining of Germanium and Silicon. *Journal of the American Ceramic Society*, 949-957.

Buijs, M., & Korpel-van Houten, K. (1993). A model for lapping of glass. *Journal of Materials Science*, 3014-3020.

Davis, G., Roblee, J., & Hedges, A. (2009). Comparison of freeform manufacturing techniques in the production of monolithic lens arrays. *SPIE Digital Library - Proceedings*, (pp. Vol.7426, pp.742605-742605-8).

Donovan, T. M., Ashley, E. J., & Bennett, H. E. (1963). Effect of Surface Damage on the Reflectance of Germanium in the 2650–10 000-Å Region. *Journal of the Optical Society of America*, 1403-1409.

Lambropoulos, J. C., Fang, T., Funkenbusch, P. D., Jacobs, S. D., Cumbo, M. J., & Golini, D. (1996). Surface microroughness of optical glasses under deterministic microgrinding. *Applied Optics*, 4448-4462.

Muralikrishnan, B., & Raja, J. (2008). *Computational surface and roundness metrology.* Springer Science & Business Media.

Nakasuji, T., Hara, S., Matsunaga, H., lkawa, N., & Shirnada, S. (1990). Diamond Turning of Brittle Materials for Optical Components. *CIRP Annals*, 89-92.

Ostojic, P., & McPherson, R. (1987). A review of indentation fracture theory: its development, principles and limitations. *International Journal of Fracture*, 297-312.

Patterson, S. R., & Magreb, E. B. (1985). Design and testing of a fast tool servo for diamond turning . *Precision Engineering*, 123–128.

APPENDIX A: SEM IMAGES

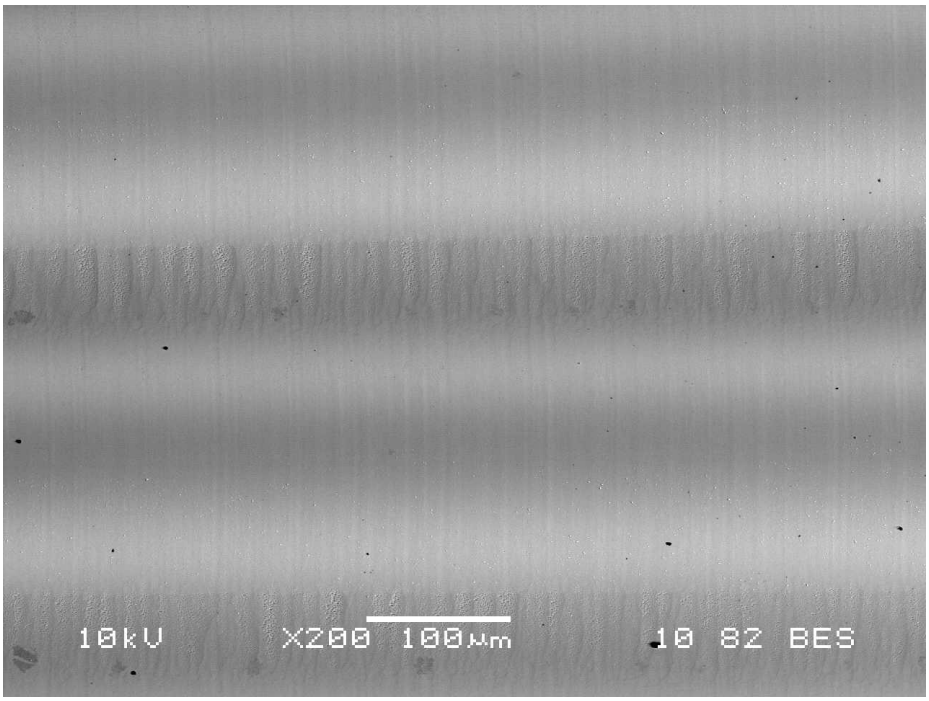

FIGURE 36: Sample 1 Right Side

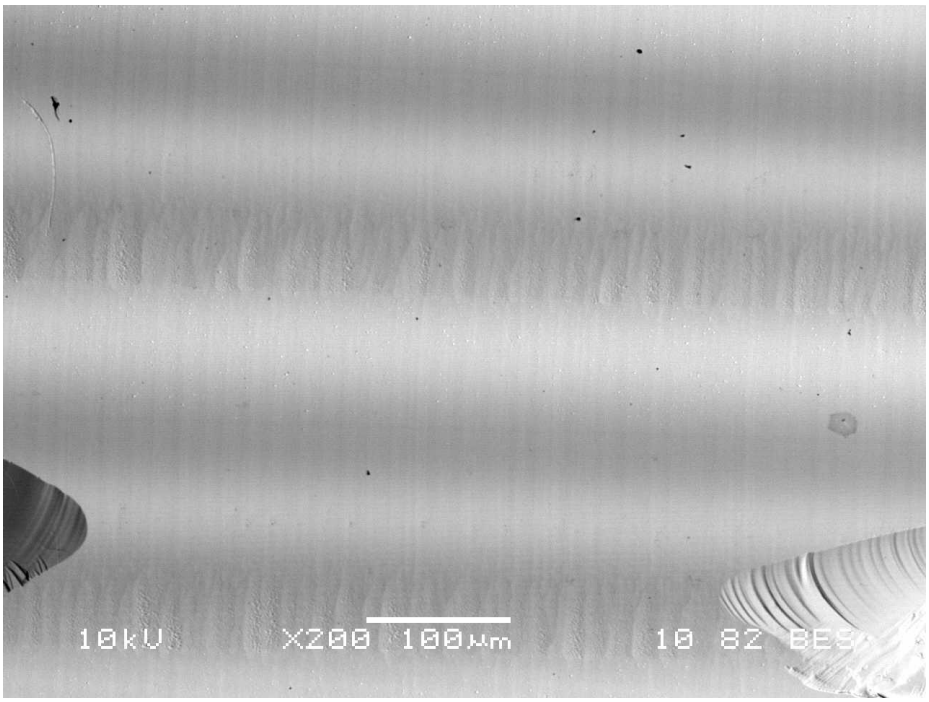

FIGURE 37: Sample 1 Left Side

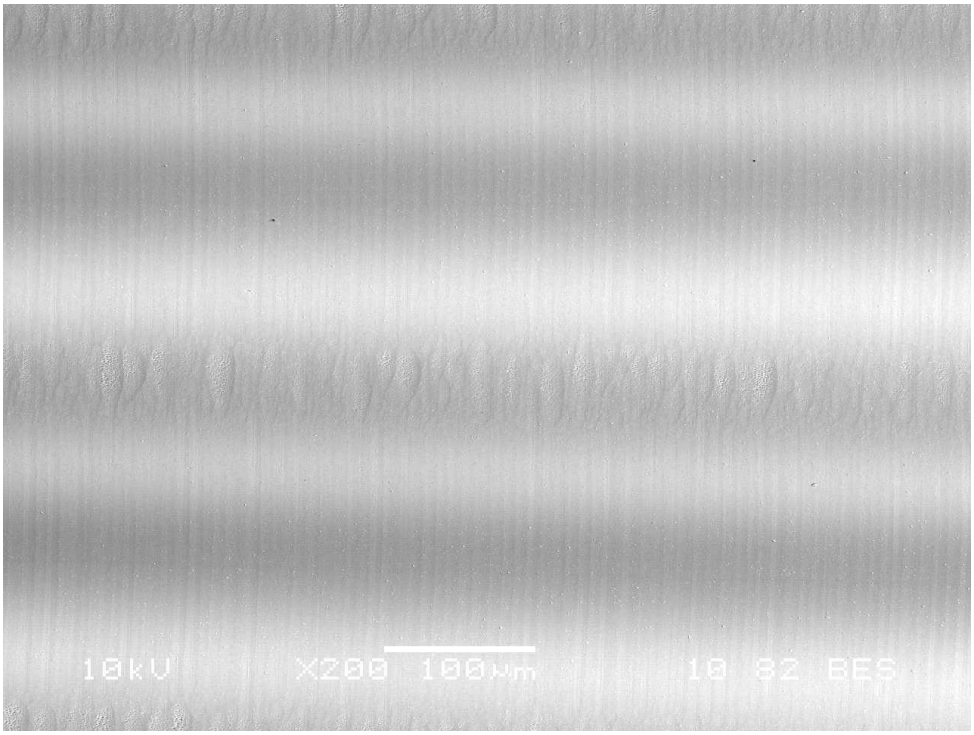

FIGURE 38: Sample 2 Right Side

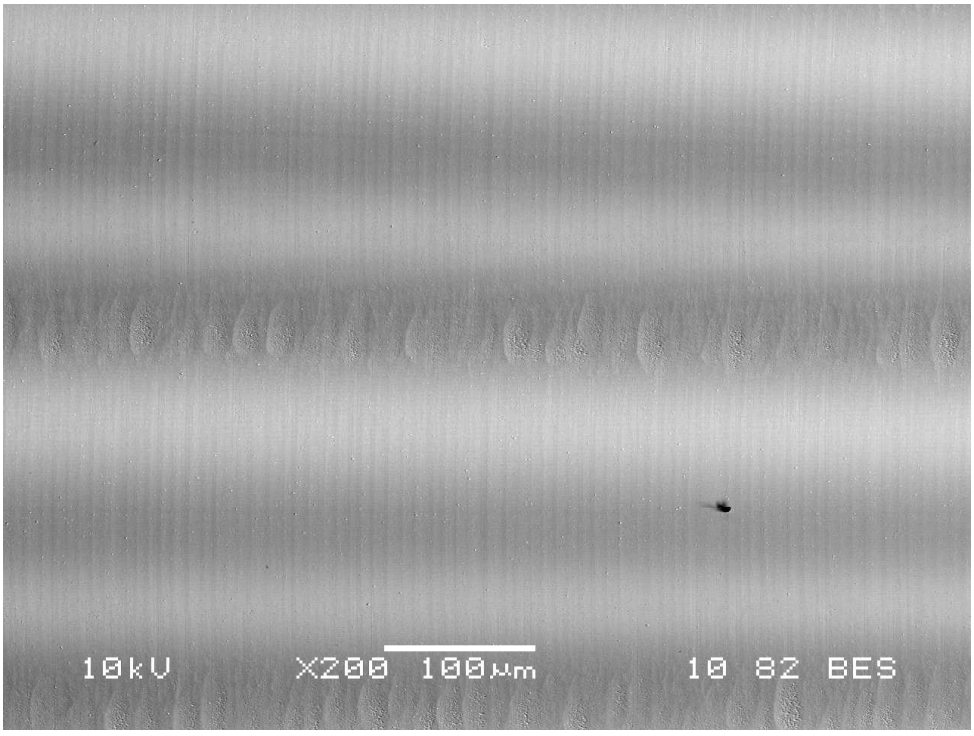

FIGURE 39: Sample 2 Left Side

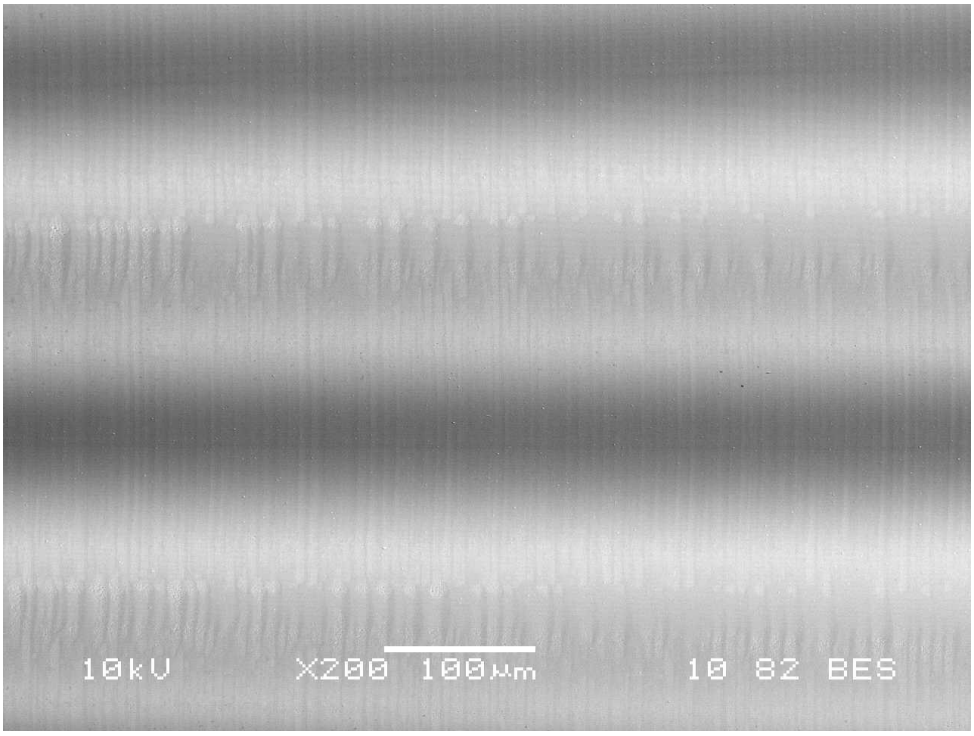

FIGURE 40: Sample 3 Right Side

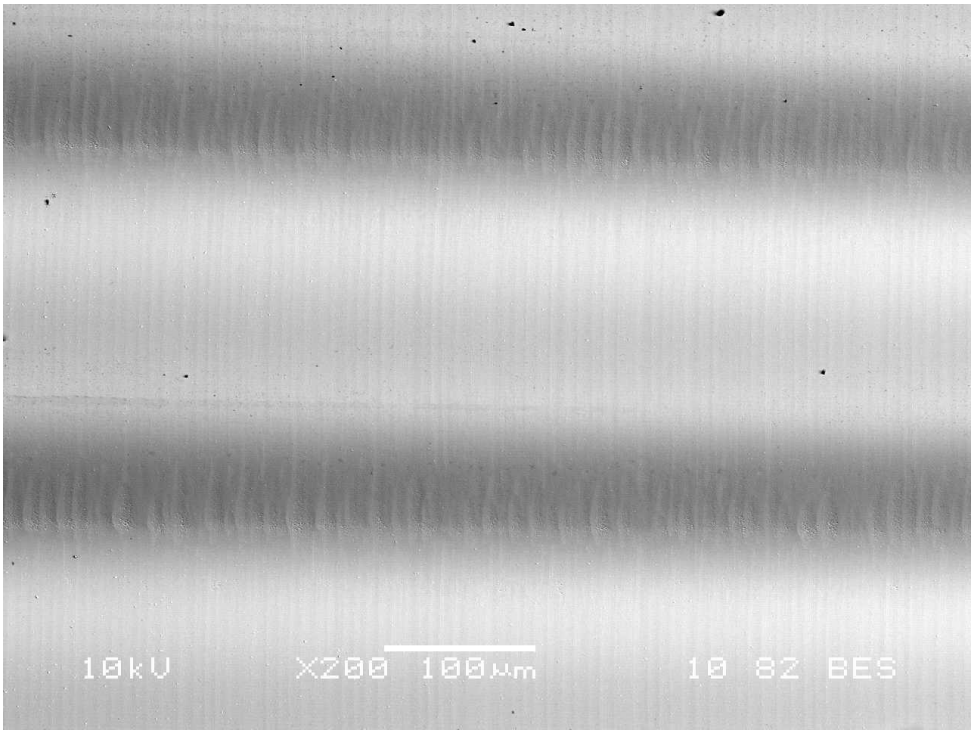

FIGURE 41: Sample 3 Left Side

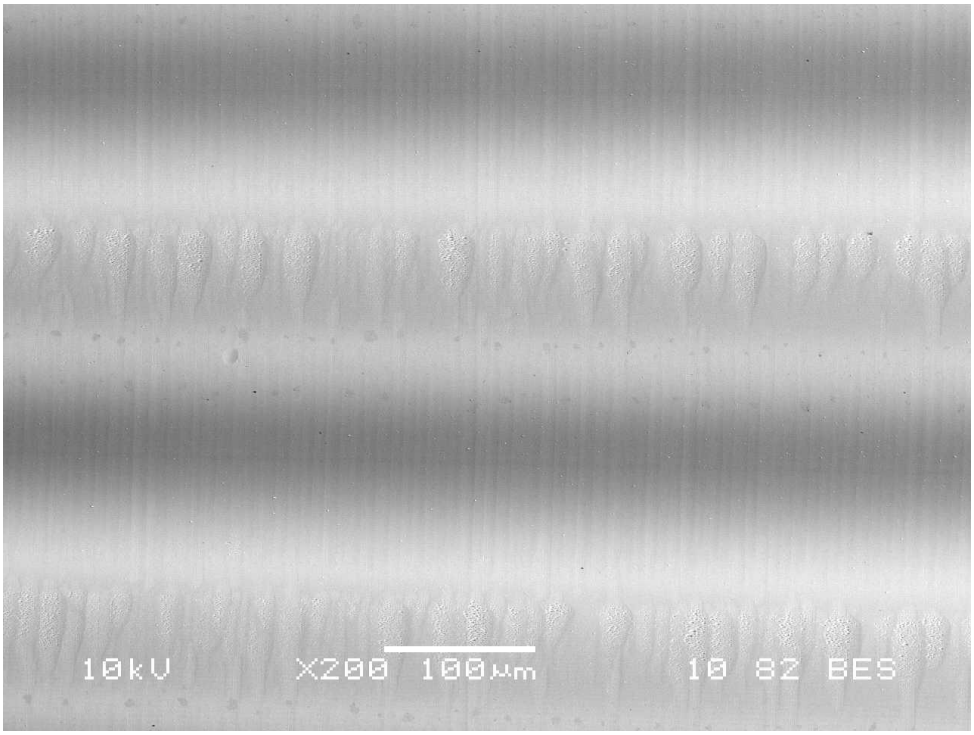

FIGURE 42: Sample 4 Right Side

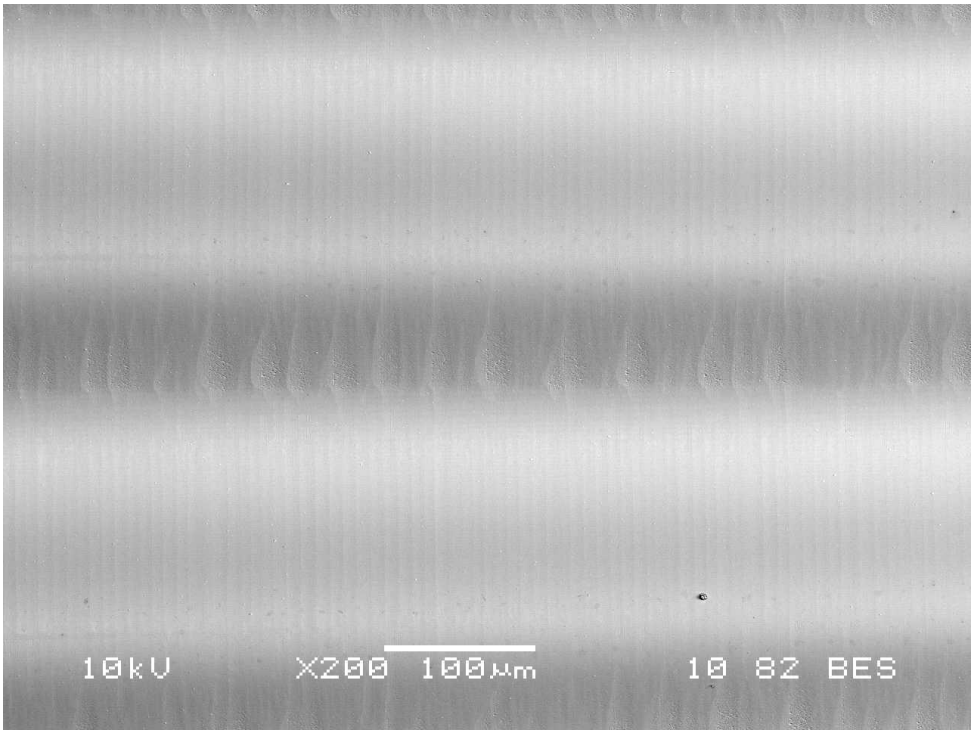

FIGURE 43: Sample 4 Left Side

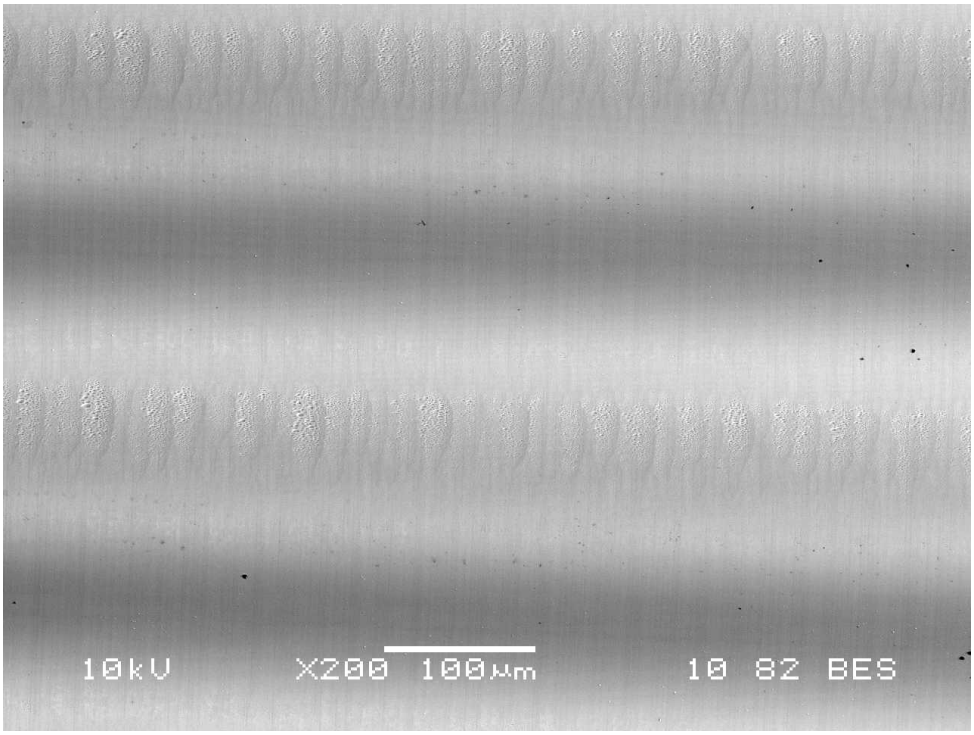

FIGURE 44: Sample 5 Right Side

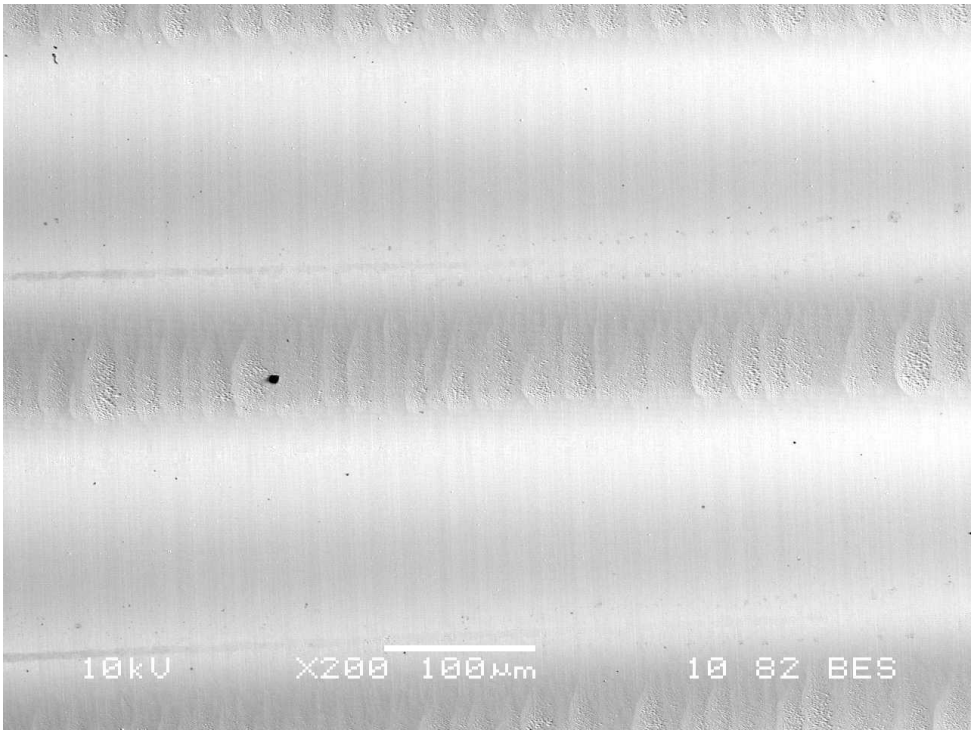

FIGURE 45: Sample 5 Left Side

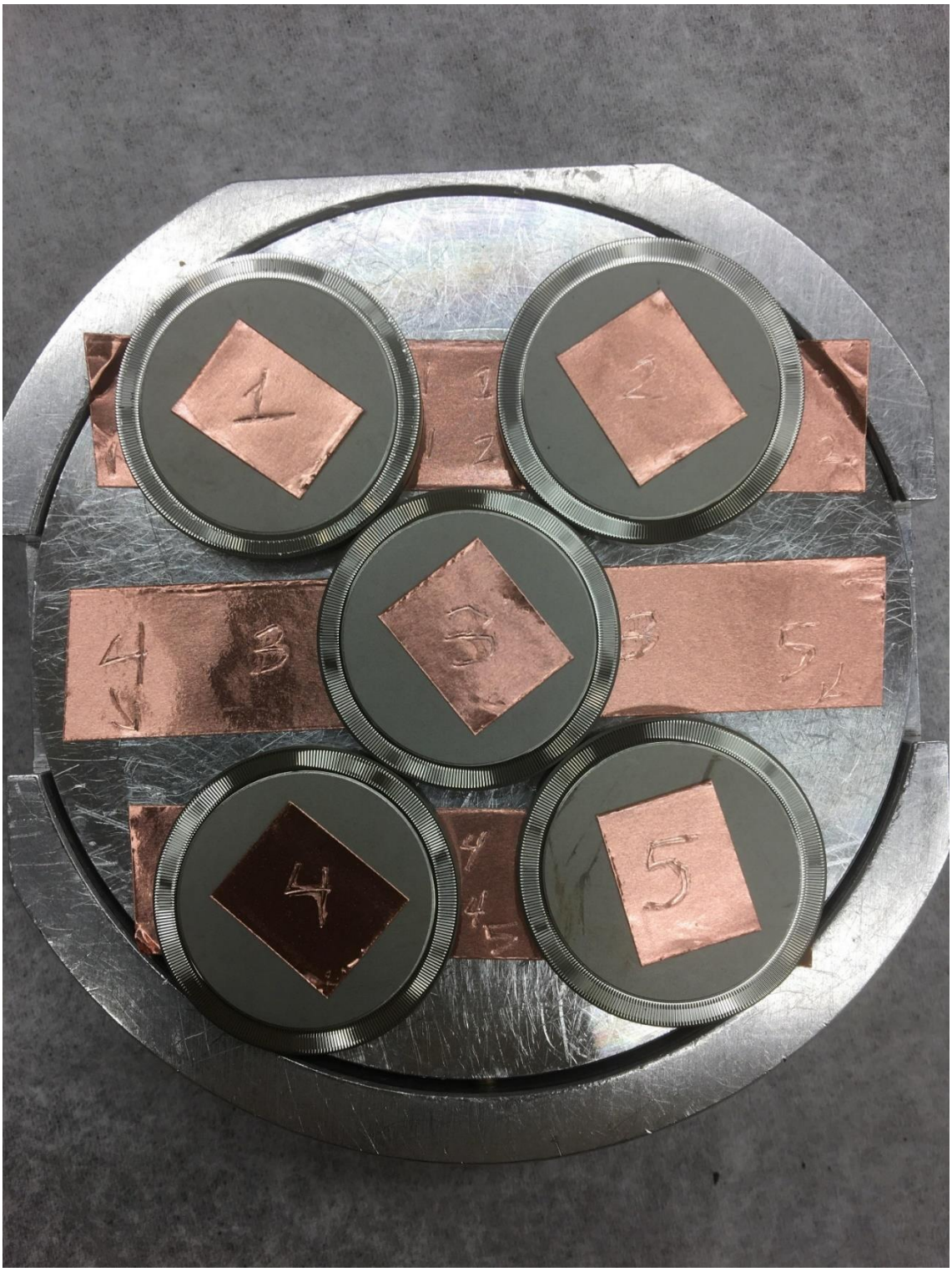

FIGURE 46: Arrangement of Samples on SEM Stage

APPENDIX B: STARBURST.M SOURCE CODE

```
%Simulation of the five optimization parts
clc;close all;clear
format long

%% Variable definition; all units in mm
partSize = 12.7;        % OR of part
OR = 12.2;              % OR of 'flat' cut area
IR = 11.2;              % IR of 'flat' cut area
cyc = 300;              % Number of cycles per rev
maxAngle = 30;          % Degrees of maximum Angle
maxAmp = tand(maxAngle)*OR/cyc;    % Maximum amplitude of the sine wave
fadeWidth = 0.5;
res = 2000;             % Simulation resolution

%% Create coordinate space
r=linspace(0,partSize,res);
[X,Y] = meshgrid(r,r);
[TH,R] = cart2pol(X,Y);

%% Remove datapoints outside part
ind = R>partSize;
TH(ind) = nan;
R(ind) = nan;

%% Calculate Z, Z prime, and Z double prime
% TH = circumference / R
%   (theta position in radians is the arclength position divided by R)
% Derivatives calculated with respect to circumference (linear tangential)
Z = (maxAmp / OR .* R) .* sin(cyc * TH);
Zp = (maxAmp / OR * cyc) .* cos(cyc * TH);
Zpp = (maxAmp / OR .* cyc .^ 2 ./ R) .* -sin(cyc * TH);

%% 'Fade' the values outside the flat area to 0
ind = R>OR & R<OR+fadeWidth; % Outer fade
fadeFactor = (OR-R(ind)+fadeWidth)/fadeWidth;
Z(ind) = Z(ind).*fadeFactor;
Zp(ind) = Zp(ind).*fadeFactor;
Zpp(ind) = Zpp(ind).*fadeFactor;

ind = R<IR & R>IR-fadeWidth; % Inner Fade
fadeFactor = (R(ind)-IR+fadeWidth)/fadeWidth;
```

```
Z(ind) = Z(ind).*fadeFactor;
Zp(ind) = Zp(ind).*fadeFactor;
Zpp(ind) = Zpp(ind).*fadeFactor;

ind = R>=OR+fadeWidth; % Outer Flat
Z(ind) = 0;
Zp(ind) = 0;
Zpp(ind) = 0;

ind = R<=IR-fadeWidth; % Inner Flat
Z(ind) = 0;
Zp(ind) = 0;
Zpp(ind) = 0;

%% Plot Z
figure
imagesc(r,r,Z)
axis image
colorbar
title('Cut Pattern (mm)')
xlabel('X(mm)')
ylabel('Y(mm)')

%% Plot angle
figure
imagesc(r,r,atand(Zp))
axis image
colorbar
title('Cut angle (deg)')
xlabel('X(mm)')
ylabel('Y(mm)')

%% Plot RoC
RoC = abs((1+Zp.^2).^(3/2)./Zpp);
RoC(abs(RoC)>1)=nan; % Remove RoC's greater than one
figure
imagesc(r,r,RoC)
axis image
colorbar
title('Cut RoC (mm)')
xlabel('X(mm)')
ylabel('Y(mm)')

%% Display max angle and min RoC
```

```
maxAngle
maxAmp
maxSag = 2*maxAmp
minRoC = nanmin(RoC(:))

%% Plot Z 3D
figure
Z(R<(IR-fadeWidth))=nan;
Z(1,1)=0;
surf(Z*500,Z,'EdgeColor','none','LineStyle','none','FaceLighting','phong')
axis image
colorbar
title('Cut Pattern (mm)')
xlabel('X(mm)')
ylabel('Y(mm)')
```

APPENDIX C: STARBURSTFORMFIT.M SOURCE CODE

```
function StarburstFormFit
clc
close all
clear

OR = 12.2;              % OR of 'flat' cut area
IR = 11.2;              % IR of 'flat' cut area
cyc = 300;              % Number of cycles per rev
maxAngle = 30;          % Degrees of maximum Angle
maxAmplitude = tand(maxAngle)*OR/cyc;    % Maximum amplitude of the sine wave

[FILENAME, PATHNAME, ~] = uigetfile('C:\Users\adgri\OneDrive\Documents\Thesis\Five
Ge Parts\NexView\*.DAT', 'Choose DAT Files to Load','MultiSelect','on');

for i = 1:length(FILENAME)
   %C(1) - Part number (1-5)
   %C(2) - Slope direction (asc/dec)
   %C(3) - Magnification (50x)
   %C(4) - Measurement number (1)
   %C(5) - Aprox cardinal position (1-4) (1=W, 2=N, 3=E, 4=S)?
   C = strsplit(FILENAME{i},{'_','.'});
   [phasemap, dx,~] = UtilityFunctions.ReadZygoBinary([PATHNAME,FILENAME{i}]);
   phasemap = phasemap * 10^3;
   dx = dx * 10^3;
   %dx=0.163e-6; % correction for ZeGage files with incorrect objective
   pixelNANs = find(isnan(phasemap));

   [nrows,ncols] = size(phasemap);
   nanmeanArray=nan(1,4);
   for j=1:length(pixelNANs)
      [row,col] = ind2sub(size(phasemap), pixelNANs(j));
      if (row<nrows)
         nanmeanArray(1) = phasemap(row+1,col);
      end
      if (row>1)
         nanmeanArray(2) = phasemap(row-1,col);
      end
      if (col<ncols)
         nanmeanArray(3) = phasemap(row,col+1);
      end
      if (col>1)
```

```
        nanmeanArray(4) = phasemap(row,col-1);
    end
    phasemap(row,col) = nanmean(nanmeanArray);
end


switch str2double(C(5))
    case 1
        positionX = -(OR + IR)/2;
        positionY = 0;
    case 2
        positionX = 0;
        positionY = (OR + IR)/2;
    case 3
        positionX = (OR + IR)/2;
        positionY = 0;
    case 4
        positionX = 0;
        positionY = -(OR + IR)/2;
end
tilt = 0;
tip = 0;
yaw = 0;

x0 = [positionX,positionY,tilt,tip,yaw];

TrialFitAnon = @(x0) TrialFit(x0,OR,cyc,maxAmplitude,phasemap,dx);

%options = optimset('Display','iter');
options.MaxIter = 5000;
options.MaxFunEvals = 10000;

options.TolFun = 1e-9;

lb = [positionX-1,positionY-1,-1,-1,-1];
ub = [positionX+1,positionY+1,1,1,1];
[converge,~,~] = fmincon(TrialFitAnon,x0,[],[],[],[],lb,ub,[],options);

x0(i,:) = converge;
positionX = converge(1);
positionY = converge(2);
tilt = converge(3);
tip = converge(4);
yaw = converge(5);
```

```
   [XPhasemap,YPhasemap] = meshgrid((0:dx:dx*(size(phasemap,1)-1)) + positionX,
(0:dx:dx*(size(phasemap,2)-1)) + positionY);

   %tilt large angle first about Y
   phasemapTilt_XZ = [cos(tilt) -sin(tilt); sin(tilt) cos(tilt)] * [XPhasemap(:)';phasemap(:)'];

   %tip small angle about X
   phasemapTip_YZ = [cos(tip) -sin(tip); sin(tip) cos(tip)] *
[YPhasemap(:)';phasemapTilt_XZ(2,:)];

   % yaw small angle about Z
   phasemapYaw_XY = [cos(yaw) -sin(yaw); sin(yaw) cos(yaw)] *
[phasemapTilt_XZ(1,:);phasemapTip_YZ(1,:)];
   X = phasemapYaw_XY(1,:);
   Y = phasemapYaw_XY(2,:);
   Z = phasemapTip_YZ(2,:);

   X = reshape(X,size(phasemap,1),size(phasemap,2));
   Y = reshape(Y,size(phasemap,1),size(phasemap,2));
   Z = reshape(Z,size(phasemap,1),size(phasemap,2));

   [TH,R] = cart2pol(X,Y);
   trialZ = (maxAmplitude / OR .* R) .* sin(cyc * TH);

   ZFormRemoved = Z-trialZ;
   ZFormRemoved = ZFormRemoved - nanmean(ZFormRemoved);
   ZLowPass = UtilityFunctions.gaussFilt3D(ZFormRemoved,dx,dx,0.015,0.015);
   ZHighPass = ZFormRemoved - ZLowPass;
   trimPixels = 50;
   ZHighPass = ZHighPass(trimPixels+1:end-trimPixels,trimPixels+1:end-trimPixels);

   figure
   subplot(1,2,1)
   imagesc(0:dx:dx*size(phasemap,1),0:dx:dx*size(phasemap,2),phasemap)
   colorbar;
   axis image
   title(strcat(FILENAME{i},'' (mm)''), 'Interpreter', 'none');
   xlabel("X (mm)");
   ylabel("Y (mm)");

   subplot(1,2,2)
   imagesc(0:dx:dx*size(ZHighPass,1),0:dx:dx*size(ZHighPass,2),ZHighPass)
   colorbar;
```

```
    axis image
    title(strcat(FILENAME{i},'' (mm)''), 'Interpreter', 'none');
    xlabel("X (mm)");
    ylabel("Y (mm)");

    SD = std(ZHighPass(:));
    avg = mean(ZHighPass(:));
    caxis([-1e-4 1e-4]);
    drawnow
end
end


function result = TrialFit(x0,OR,cyc,maxAmplitude,phasemap,dx)
positionX = x0(1);
positionY = x0(2);
tilt = x0(3);
tip = x0(4);
yaw = x0(5);

[XPhasemap,YPhasemap] = meshgrid((0:dx:dx*(size(phasemap,1)-1)) + positionX,
(0:dx:dx*(size(phasemap,2)-1)) + positionY);

%tilt large angle first about Y
phasemapTilt_XZ = [cos(tilt) -sin(tilt); sin(tilt) cos(tilt)] * [XPhasemap(:)';phasemap(:)'];

%tip small angle about X
phasemapTip_YZ = [cos(tip) -sin(tip); sin(tip) cos(tip)] *
[YPhasemap(:)';phasemapTilt_XZ(2,:)];

% yaw small angle about Z
phasemapYaw_XY = [cos(yaw) -sin(yaw); sin(yaw) cos(yaw)] *
[phasemapTilt_XZ(1,:);phasemapTip_YZ(1,:)];
X = phasemapYaw_XY(1,:);
Y = phasemapYaw_XY(2,:);
Z = phasemapTip_YZ(2,:);

X = reshape(X,size(phasemap,1),size(phasemap,2));
Y = reshape(Y,size(phasemap,1),size(phasemap,2));
Z = reshape(Z,size(phasemap,1),size(phasemap,2));

[TH,R] = cart2pol(X,Y);
trialZ = (maxAmplitude / OR .* R) .* sin(cyc * TH);
```

```
mapDiff = Z-trialZ;
result = nanstd(mapDiff(:));
end
```

APPENDIX D: MAHRANALYSIS.M SOURCE CODE

```
clc; close all;

%loop through mahr loaded into workspace
for j=1:5
   switch j
      case 1
         X=X1;
         Z=Z1;
      case 2
         X=X2;
         Z=Z2;
      case 3
         X=X3;
         Z=Z3;
      case 4
         X=X4;
         Z=Z4;
      case 5
         X=X5;
         Z=Z5;
   end

   %set pixel spacing
   P = 0.2461;
   offset = -0.02+P/2;
   Xtemp = (X+offset)/P;
   Xfloor = floor(Xtemp);
   Xrem = (Xtemp-Xfloor)*P;
   pause on

   %create ideal profile to match to measured profile
   Xp = linspace(-pi/2,3*pi/2,247);
   Yp = 0.046 * sin(Xp);
   Ya = 30*cos(Xp);

   %loop through measured data and find places where local form matches
   %prescription
   SD=nan(size(X));
   for i=124:length(X)-123
      SD(i)=std(Z(i-123:i+123)-Yp(:));
   end
```

```
TF = islocalmin(SD);
TF(SD>0.02)=0;
ind = find(TF);

amplitude = 0.0455/2;

form = amplitude * cos(pi*(-0.123:0.001:0.123)/0.123)';

%loop through and filter the found segments
segments = nan(247,length(ind));
segmentsFormRemoved = segments;
segmentsFiltered = segments;
for i=1:length(ind)
   tempSegment = Z((ind(i)-123):(ind(i)+123));
   tempSegment = tempSegment - mean(tempSegment);
   segments(:,i) = tempSegment;
   segmentsFormRemoved(:,i) = tempSegment - form;
   segmentsFiltered(:,i) = segmentsFormRemoved(:,i) -
UtilityFunctions.gaussFiltRobust(segmentsFormRemoved(:,i),0.001,1/0.015);
   segmentsFiltered(:,i) =
UtilityFunctions.gaussFiltRobust(segmentsFiltered(:,i),0.001,1/0.002);
end

%exclude outliers
overallSTD = std(segmentsFiltered)';
excludeIND = overallSTD>(mean(overallSTD)+1*std(overallSTD));
overallSTD(excludeIND) = [];
segments(:,excludeIND) = nan;
segmentsFormRemoved(:,excludeIND) = nan;
segmentsFiltered(:,excludeIND) = nan;
theta = mod(X/(2*pi*11.749),1)*360;
theta = theta(ind);
theta(excludeIND) = [];


%Perform all plotting
figure(1)
subplot(5,1,j)
for i=1:length(ind)
   plot(-0.123:0.001:0.123,segments(:,i))
   hold on
end
xlabel("Segment X (mm)")
ylabel("Segment Y (mm)")
```

```
    title(sprintf("Sample %d Segments",j))
    xlim([-0.123 0.123]);
    ylim([-0.025 0.025]);

    figure(2)
    subplot(5,1,j)
    for i=1:length(ind)
        plot(-0.123:0.001:0.123,segmentsFiltered(:,i))
        hold on
    end
    xlabel("Segment X (mm)")
    ylabel("Segment Y (mm)")
    title(sprintf("Sample %d Filtered Segments",j))
    xlim([-0.123 0.123]);
    ylim([-0.0003 0.0003]);

    [~,overlapIND] = max(theta);

    figure(3)
    subplot(5,1,j)
    plot(theta(1:overlapIND), overallSTD(1:overlapIND))
    hold on
    plot(theta(overlapIND+1:end), overallSTD(overlapIND+1:end),'r')

    xlabel("Segment Azimuth Position (deg)")
    ylabel("Filtered Segment RMS (mm)")
    title(sprintf("Sample %d Segment RMS vs Azimuth Position",j))
    xlim([0 360]);
    ylim([0.000005 0.00005]);
end
```